Models of large-scale viscous flow in the Earth's mantle with constraints from mineral physics and surface observations

Bernhard Steinberger[1] and Arthur R. Calderwood[2]

[1]*Center for Geodynamics, NGU,* N-7491 *Trondheim, Norway. E-mail: bernhard.steinberger@ngu.no*
[2]*Sauder School of Business, University of British Columbia, Vancouver, BC, Canada* V6T 1Z2

SUMMARY
Modelling the geoid has been a widely used and successful approach in constraining flow and viscosity in the Earth's mantle. However, details of the viscosity structure cannot be tightly constrained with this approach. Here, radial viscosity variations in four to five mantle layers (lithosphere, upper mantle, one to two transition zone layers, lower mantle) are computed with the aid of independent mineral physics results. A density model is obtained by converting *s*-wave anomalies from seismic tomography to density anomalies. Assuming both are of thermal origin, conversion factors are computed based on mineral physics results. From the density and viscosity model, a model of mantle flow, and the resulting geoid and radial heat flux profile are computed. Absolute viscosity values in the mantle layers are treated as free parameters and determined by minimizing a misfit function, which considers fit to geoid, 'Haskell average' determined from post-glacial rebound and the radial heat flux profile and penalizes if at some depth computed heat flux exceeds the estimated mantle heat flux 33 TW. Typically, optimized models do not exceed this value by more than about 20 per cent and fit the Haskell average well. Viscosity profiles obtained show a characteristic hump in the lower mantle, with maximum viscosities of about 10^{23} Pa s just above the D″ layer— several hundred to about 1000 times the lowest viscosities in the upper mantle. This viscosity contrast is several times higher than what is inferred when a constant lower mantle viscosity is assumed. The geoid variance reduction obtained is up to about 80 per cent—similar to previous results. However, because of the use of mineral physics constraints, a rather small number of free model parameters is required, and at the same time, a reasonable heat flux profile is obtained. Results are best when the lowest viscosities occur in the transition zone. When viscosity is lowest in the asthenosphere, variance reduction is about 70–75 per cent. Best results were obtained with a viscous lithosphere with a few times 10^{22} Pa s. The optimized models yield a core-mantle boundary excess ellipticity several times higher than observed, possibly indicating that radial stresses are partly compensated due to non-thermal lateral variations within the lowermost mantle.

Key words: geoid, heat flow, mantle convection, mantle viscosity, mineralogy, tomography.

GJI Tectonics and geodynamics

1 INTRODUCTION

Mantle rheology is still one of the rather poorly known properties of the Earth. It is widely agreed upon that, below a brittle lithospheric layer, mantle rocks behave, on timescales of thousands or millions of years, like a highly viscous fluid. Viscous flow in the Earth's mantle is presumably the principal way how the Earth transports heat through the bulk mantle, and an underlying cause for gravity and geoid undulations, tectonic plate motions as well as stresses in the Earth's lithosphere.

Research efforts to determine mantle viscosity can be broadly divided into three areas: (i) mineral physics, (ii) post-glacial rebound and (iii) large-scale mantle flow.

Determining viscosity from mineral physics alone is difficult, because different deformation mechanisms—diffusion creep and dislocation creep—may play a role. For either mechanism, the effective viscosity depends on a number of factors—such as temperature, grain size, water content, etc., and many of these are poorly known.

Measurement of post-glacial rebound has been the classical method of determining mantle viscosity ever since the canonical value of 10^{21} Pa s was established by Haskell (1935). Newer results (e.g. Mitrovica 1996; Lambeck & Johnston 1998) confirm this, and additionally also indicate a viscosity increase with depth; however, they also show that post-glacial rebound cannot resolve details of mantle viscosity structure, and is particularly insensitive to viscosity below about 1400 km depth.

Mantle flow can be computed, if density field, viscosity structure, etc., are known, and comparison of computed advected heat flux, plate motions, geoid, stresses, etc., with observations can help to assess the 'success' of the model, and thus help to constrain viscosity and other properties on which the results depend. For simplicity and computational efficiency, the assumption of radial viscosity variations only is frequently made. In this case, density and flow field can be expanded in spherical harmonics, and computed separately for each degree and order, using a formalism developed by Hager & O'Connell (1979, 1981). This formalism was extended by Ricard *et al.* (1984) and Richards & Hager (1984) to the computation of the geoid. Since then, the geoid (which is extremely well known compared to other quantities that can be used) has been taken as a constraint to mantle viscosity and flow in numerous publications. These essentially show that large parts of the geoid can be explained based on viscous flow models with radial viscosity variations only. Thoraval & Richards (1997) review this body of publications; however, they also show that the geoid alone cannot give a very tight constraint on mantle flow and the quantities on which it depends, such as viscosity and density anomalies, and the only robust result is, that a substantial viscosity increase with depth is required to fit the geoid data. Including lateral variations in viscosity was found not improve the fit to the geoid (Zhang & Christensen 1993). More recently, Čadek & Fleitout (2003, 2006), however, found that the fit can be improved by including lateral viscosity variations in the top 300 km, and close to the core–mantle boundary (CMB). Also on a regional scale, lateral viscosity variations appear to be important in determining the mantle flow field (Albers & Christensen 2001).

Because of the limitations of each individual method, the need to jointly fit several observations and incorporate other data to constrain viscosity and other properties that determine flow in the Earth's mantle became apparent. Mitrovica & Forte (1997) jointly fit the geoid and post-glacial rebound observables, and confirm a significant increase of viscosity with depth. Pari & Peltier (1995) use heat flow constraints in addition to the geoid. Other quantities considered include plate motions (e.g. Ricard & Vigny 1989; Lithgow-Bertelloni & Richards 1998; Becker & O'Connell 2001; Conrad & Lithgow-Bertelloni 2002, 2004), dynamic surface topography (Lithgow-Bertelloni & Silver 1998; Kaban *et al.* 1999; Pari & Peltier 2000; Panasyuk & Hager 2000; Steinberger *et al.* 2001; Čadek & Fleitout 2003), CMB topography and ellipticity (Forte *et al.* 1993, 1995) and lithospheric stresses (Ricard *et al.* 1984; Bai *et al.* 1992; Steinberger *et al.* 2001; Lithgow-Bertelloni & Guynn 2004) or a combination of several of these (Mitrovica & Forte 2004). However, none of these quantities is as accurately known as the geoid.

In order to optimize the fit to these various observations, a large number of parameters can be adjusted, and the task of mantle flow modelling with observational constraints can thus become rather complex. In order to reduce the number of parameters it is, therefore, useful to consider constraints from mineral physics as well.

Here we will derive flow models making these simplifying assumptions: (1) Both lateral density and seismic velocity variations are due to temperature variations; the conversion factors between these variations depend only on depth, hence tomography models can be converted to density models. (2) Mantle viscosity only depends on depth. We will then use an adiabatic thermal profile with boundary layers and results from mineral physics to derive viscosity and conversion factors as a function of depth. We will derive relative viscosity variations in mantle layers with approximately constant mineralogy (upper mantle, one or two layers in transition zone, lower mantle) and leave absolute values as free parameters. In

addition, we will keep the lithospheric viscosity as a free parameter. This is necessary in order to compensate for the fact that the viscous rheology used here is not appropriate for the lithosphere. A more realistic treatment is difficult, we still lack a detailed knowledge of lithospheric rheology, and self-consistent models of plate tectonics are only beginning to emerge. The optimized lithospheric viscosity obtained in that way represents an effective viscosity along plate boundaries, where most of the lithospheric deformation occurs. This is much less than what is generally thought to be appropriate for plate interiors. We will then use density models inferred from seismic tomography in combination with viscosity models to compute mantle flow. The geoid is computed from density anomalies and deformation of boundaries caused by the flow. The radial heat flux profile is computed from the flow and density variations converted back to temperature variations. Our optimization is done by minimizing a misfit function that is computed based on

   (i) the difference between predicted and observed geoid
   (ii) compatibility of viscosity structure with post-glacial rebound results
   (iii) compatibility of radial heat flux profile with observations

Plate velocity predictions as well as predictions of lithospheric stress and dynamic topography turn out to be rather insensitive to variations of viscosity with depth (Becker & O'Connell 2001; Steinberger *et al.* 2001); therefore, we do not use these in our optimization. For models with lateral viscosity variations, though, Conrad & Lithgow-Bertelloni (2006) recently showed that deeply penetrating continental roots increase the magnitude of shear tractions that mantle flow exerts on the base of Earth's lithosphere by a factor of 25, compared to a 100-km-thick lithosphere.

Obviously, there are also other uncertainties than absolute viscosity values, which are free parameters of our optimization. We will treat those by modifying other model parameters relative to the reference model and discussing how results change. Model parameters are listed in Table 1.

In the next chapter, we will discuss how we derive the viscosity and scaling factor profiles from mineral physics. After this, the computation of mantle flow, geoid and advected heat flux, and how the misfit function is constructed, is explained. We will then present results. We will also discuss some '*a posteriori*' predictions of quantities that were not used in the optimization—surface motion and CMB excess ellipticity (Mathews *et al.* 2002). This will point towards shortcomings of this work, and future improvements.

In particular, there has been recently increasing evidence (e.g. Masters *et al.* 2000; Trampert *et al.* 2004; Ishii & Tromp 2004) that probably not all seismic velocity anomalies are due to temperature anomalies, as assumed here. The approach taken here is to test how well observations can be fit under the assumption that seismic velocity anomalies are caused by temperature anomalies, and how we have to choose modelling parameters in order to obtain an optimum fit. We test a range of *s*-wave tomographic models (Becker & Boschi 2002; Ritsema & van Heijst 2000; Masters *et al.* 2000; Grand 2002; Mégnin & Romanowicz 2000; Su *et al.* 1994; Gu *et al.* 2001). This approach actually yields additional evidence for chemical heterogeneities, as will be explained in more detail below, and discussed further elsewhere (Steinberger & Holme 2006).

2 MINERAL PHYSICS THEORY

In this chapter we discuss (if adopted from elsewhere) or derive parameters used in our model. They are assumed either constant or depth dependent and listed alphabetically in Table 1. We will first

Table 1. Model parameters. For constant parameters, values are given for reference model, followed by alternative values (model number in brackets), followed by range covered in contour plots, unless they are allowed to vary in the optimization.

Symbol	Value	Depth (range)	Name and/or comment
a_0	2.9; 3.5 (M2); 2–4	>660 km	Thermal expansivity coefficient (eq. 17)
a_1	0.9	>660 km	Thermal expansivity coefficient (eq. 17)
b	1.4; 0 (M4)	>660 km	Specifies depth dependence of α (eq. 15)
	0	<660 km	
C_p	1250 J kg^{-1} K^{-1}		Specific heat
$d_{D''}$	200 km; 100–350 km	>2541 km	Thickness of bottom thermal boundary layer
d_{lith}	100 km	<100 km	Thickness of top thermal boundary layer
$(\partial \ln v_{s,0}/\partial T)_p$	Fig. 5		See Section 2.5
$\frac{d\mu_0}{dT}$	27 MPa K^{-1}	>660 km	Temperature derivative of shear modulus at $p=0$
F_l	0.5; 0–1	<220 km	Conversion factor reduction relative to Fig. 6
g	12; 30; 20 (M2,5); 4–70	>660 km	Relates H and T_m (eq. 10), thus influences scaling factor profile through eq. (22)
$g'(= g/n)$	12; 20 (M5); 4–20	>660 km	Determines steepness of viscosity profile (eq. 11)
H	Fig. 1		Activation enthalpy
n	1; 2.5 (M2); 1–3.5	>660 km	Stress exponent
	3.5	<660 km	
p			Pressure
q_i	Allowed to vary in optimization		Determine absolute viscosity (eq. 19)
Q	See Section 2.5		Seismic Q-factor
R	8.3144 J K^{-1} mol^{-1}		Universal gas constant
$\overline{T}$	Fig. 2		(Laterally averaged) temperature
T_0	285 K	0 km	Surface temperature
T_{CMB}	3500 K; 3000–4000 K	2891 km	Temperature at core–mantle boundary
$T_{lm,0}$	See Section 2.5	>660 km	Lower mantle potential surface temperature
T_m	Figs. 1, 2		Melting temperature
$T_{um,0}$	1613 K	<400 km	(Upper mantle) potential surface temperature
α	Fig. 3		Thermal expansivity
γ	From PREM		gravity
$\Gamma\Delta\rho$	$-0.3 \cdot 10^3$ MPa K$^{-1} \cdot$ kg m^{-3}	660 km	Product of Clapeyron slope and density jump
	$0.5 \cdot 10^3$ MPa K$^{-1} \cdot$ kg m^{-3}	400 km	at phase boundary
δ_{T0}	5.5		Specifies depth dependence of α (eq. 15)
$\tilde{\eta}$	Fig. 4		Normalized viscosity
μ	From PREM		Shear modulus
ρ	From PREM		Actual density
ρ_0	See Section 2.3		Density extrapolated to zero pressure

discuss the viscosity law in general (Section 2.1.1) and restricted to only radial viscosity variations (Section 2.1.2). This is followed by a discussion of the parameters involved. These include the stress exponent n, activation enthalpy H, melting temperature T_m and the factors g and g' (Section 2.2), as well as a number of further parameters that determine the radial profiles of laterally averaged temperature $\overline{T}$ and thermal expansivity α (derived jointly in Section 2.3), as well as the viscosity scaling factors (Section 2.4) which are treated as free parameters in the optimization. We further discuss parameters affecting the relation between seismic velocity and temperature anomalies (Section 2.5) and the factor F_l used to adjust the relation between seismic velocity and density variations in the uppermost mantle.

2.1 Mantle viscosity

Our numerical flow model will only consider radially varying, Newtonian viscosity, however, in order to derive the appropriate viscosity profile, and in order to make our derivation extendable to more realistic rheologies, we keep it rather general.

2.1.1 General rheological model

We adopt the frequently used approach of assuming a power-law rheology, where the relation between strain rate $\dot{\epsilon}$ and stress σ (more specifically, the square root of the second invariant of the respective tensors) is of the form

$$\dot{\epsilon} = C_1 \sigma^n \exp\left(-\frac{H}{RT}\right),\qquad(1)$$

whereby H is activation enthalpy, R is the universal gas constant, T is temperature and C_1 is a constant. Solving the equation for σ gives

$$\sigma = \dot{\epsilon}^{\frac{1}{n}} \cdot \frac{1}{C_1^{\frac{1}{n}}} \exp\left(\frac{H}{nRT}\right).\qquad(2)$$

With the usual definition of viscosity η, it follows

$$\eta = \frac{\sigma}{2\dot{\epsilon}} = \dot{\epsilon}^{\frac{1}{n}-1} \cdot \frac{1}{2C_1^{\frac{1}{n}}} \exp\left(\frac{H}{nRT}\right).\qquad(3)$$

In order to avoid the singularity $\eta \longrightarrow \infty$ for $\dot{\epsilon} \longrightarrow 0$ we replace $\dot{\epsilon}^{\frac{1}{n}-1}$ with $\left(\frac{\dot{\epsilon}^2}{\langle\dot{\epsilon}^2\rangle(z)} + \dot{\epsilon}_0^2\right)^{\frac{1-n}{2n}} \cdot (\langle\dot{\epsilon}^2\rangle(z))^{\frac{1-n}{2n}}$. Here $\langle\dot{\epsilon}^2\rangle(z)$ is the laterally averaged second invariant of the strain rate tensor which only depends on the radial coordinate z, and $\dot{\epsilon}_0$ is a number smaller than 1. T is split up into a laterally averaged part $\overline{T}(z)$ which only depends on z, and the 'temperature anomaly' δT:

$$\frac{1}{T} = \frac{1}{\overline{T} + \delta T} = \frac{1}{\overline{T}} - \frac{\delta T}{\overline{T}(\overline{T} + \delta T)}.\qquad(4)$$

We can then write viscosity as

$$\eta = \eta_i \cdot V_{rT}(z) \cdot V_{rs}(z) \cdot V_{lT} \cdot V_{ls}, \tag{5}$$

$$V_{lT} = \exp\left(-\frac{H\delta T}{nR\overline{T}(\overline{T}+\delta T)}\right) \quad \text{and} \quad V_{ls} = \left(\frac{\dot{\epsilon}^2}{\langle\dot{\epsilon}^2\rangle(z)} + \epsilon_0^2\right)^{\frac{1-n}{2n}}, \tag{6}$$

are the lateral variation of viscosity due to lateral temperature and strain rate variations and are not considered in our flow computation. We continue now with discussing η_i, V_{rT} and V_{rs} which determine the radial viscosity profile.

2.1.2 Radial viscosity profile—equations

η_i are called 'anchor viscosities' and are adjusted such as to minimize the misfit between model predictions and observations as described below. They are determined independently for various depth ranges for which different phase assemblages occur (upper mantle, one to two layers in transition zone, lower mantle).

$$V_{rT}(z) = \exp\left(\frac{H(z)}{nR\overline{T}(z)}\right), \tag{7}$$

is the radial variation of viscosity due to radial temperature and pressure variations at constant strain rate and

$$V_{rs}(z) = (\langle\dot{\epsilon}^2\rangle(z))^{\frac{1-n}{2n}}, \tag{8}$$

is the radial variation of viscosity due to strain rate variations.

Similarly, it can be shown that for constant stress $\eta \sim \exp(H/(RT))$ and for constant dissipation rate $\eta \sim \exp(2H/((n+1)RT))$. In other words, effective viscosity can be expressed in the form

$$\eta \sim \exp\left(\frac{rH}{R\overline{T}}\right), \tag{9}$$

with $r = 1/n$ for constant strain rate, $r = 2/(n+1)$ for constant dissipation rate and $r = 1$ for constant stress. For Newtonian viscosity ($n = 1$) it is $r = 1$ in all cases. Christensen (1983) showed for 2-D numerical experiments that the properties of non-Newtonian flow with $n = 3$ can be closely imitated by Newtonian flow with activation enthalpy reduced by a factor $r = 0.3$–0.5. Thus the appropriate viscosity dependence appears to be somewhere between constant strain rate and constant dissipation rate. Here we use the constant strain rate formulation, that is, eq. (7) and $V_{rs} = 1$. We consider this appropriate for the purpose of this paper, for the following reasons:

(i) For the lower mantle, we will explicitly discuss the dependence of results on the reduction factor r (expressed in terms of g'). Our reference case is with $n = 1$ (Newtonian viscosity), however, given the results of Christensen (1983), our results are probably applicable to the case of non-Newtonian viscosity as well.

(ii) For the mantle above 660 km it will turn out that the resulting optimized viscosity profile is mainly determined by the anchor viscosities, and results are rather insensitive to the factor r. In particular, we will show that results remain rather similar regardless of whether variations in viscosity due to variations in temperature and activation enthalpy in the upper mantle and transition zone layers are considered or whether constant viscosity is assumed within these layers.

We will now discuss the stress exponent n and profiles $H(z)$ and $\overline{T}(z)$.

2.2 Stress exponent, activation enthalpy and melting temperature

2.2.1 Stress exponent

The appropriate value for the stress exponent n is not well known, since solid-state flow in the mantle can be achieved through both dislocation creep and diffusion creep. For dislocation (or power-law) creep, $n \approx 3.5$ is usually considered appropriate, whereas $n = 1$ for diffusion creep. Power-law creep is favoured for high stresses, large grain sizes, high temperatures and low pressures, whereas diffusion creep for low stresses, small grain sizes, low temperatures and high pressures. It is thought that both mechanisms may contribute to flow in the upper mantle, with composite viscosity intermediate, but laboratory studies favour dislocation creep in the shallow upper mantle (Ranalli 1995; Schubert *et al.* 2001). Further evidence for dislocation creep in the upper mantle comes from geodynamic modelling (van Hunen *et al.* 2005). Ranalli (1995) concludes on p. 390 that 'if there is no thermal boundary layer (TBL) between upper and lower mantle (mantle-wide convection) power-law creep is predominant in the lower mantle'. On the other hand, the fact that the lower mantle is nearly isotropic, has been interpreted such that diffusion creep is the dominant deformation mechanism (Karato *et al.* 1995), at least above the D″ layer. As reference case will use eq. (7) with $n = 3.5$ above 660 km and $n = 1$ below.

2.2.2 Activation enthalpy

Activation enthalpy H is the sum of activation energy plus pressure times activation volume. Kohlstedt and Goetze (1974) determined activation energy 525 kJ mol^{-1} for dislocation (power-law) creep in dry olivine. Activation volume is more uncertain. Above 660 km, we will use the continuous line in Fig. 1 as reference case profile
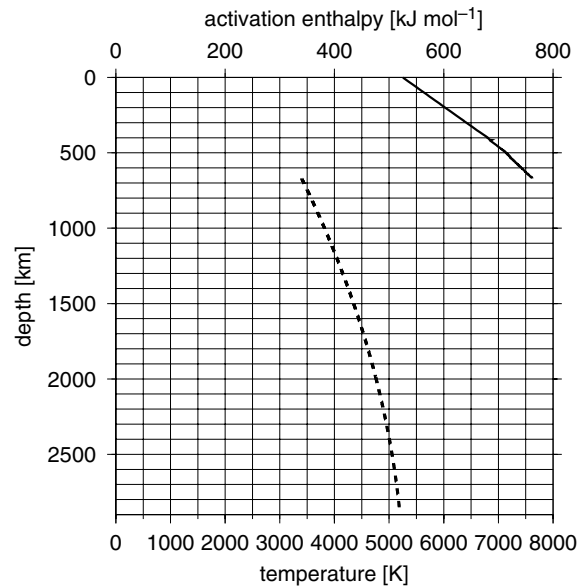
Figure 1. Solid line—upper scale: activation enthalpy profile based on Calderwood (1999) used in the upper mantle. dashed line—lower scale: lower mantle melting temperature profile used, intermediate between the curves determined for MgSiO$_3$ perovskite (Wang 1999) and MgO (Zerr & Boehler 1994). The two scales differ by a factor $gR = 100$ J mol^{-1} K corresponding to $g = 12$. In this way, the curve for the lower mantle can be also used with the upper scale and upper mantle viscosity law to determine lower mantle viscosity and vice versa.

for activation enthalpy. It is based on Calderwood (1999) and very similar to a $H(z)$ profile given by Ranalli (1995).

For zero depth, it equals the value determined by Kohlstedt & Götze (1974). Its increase with depth corresponds to an activation volume of about 12 cm^3 mol^{-1} at depth 100 km, decreasing to 10 cm^3 mol^{-1} at depth 660 km—within the range of experimental results. Since upper mantle viscosities are mainly determined by the anchor viscosities, and rather insensitive to the activation enthalpy profile, we shall not discuss it in more detail.

2.2.3 Melting temperature

The activation enthalpy profile is mainly important for determining the viscosity profile in the lower mantle. Weertman & Weertman (1975) give an empirical relation

$$H = gRT_m, \tag{10}$$

whereby g is a dimensionless constant, and T_m is melting temperature. Then eq. (7) becomes

$$F_{rT}(z) = \exp\left(\frac{g' \cdot T_m(z)}{\overline{T}(z)}\right), \tag{11}$$

with $g' = g/n$. In the reference case for the lower mantle, we will use eq. (11) with $g' = 12$, the arithmetic mean of values determined by Yamazaki & Karato (2001) for silicon diffusion in MgSiO$_3$ perovskite and MgO. However, we will consider other values as well, and emphasize that our reference value may also correspond to effective viscosity for power-law creep with larger g.

Experimental values exist for the the melting curves of lower mantle constituents MgSiO$_3$ perovskite (Wang 1999) and MgO (Zerr & Boehler 1994). Yamazaki & Karato (2001) consider using the melting curves of these constituents—which both look similar—appropriate. Here, a melting curve intermediate between those two curves (see Fig. 1) is used.

2.3 Mantle temperature and thermal expansivity

The radial temperature profile is also required to derive viscosity as a function of depth. We assume here the temperature profile is adiabatic except for TBLs. This is not standard practice in the geodynamical literature—the adiabatic gradient is generally removed because it does not influence the dynamics directly. However, it does influence the mineral physics constraints on material properties, which is why it is included here. A number of further parameters are involved here. These can be grouped into those determining the adiabatic temperature gradient (thermal expansivity $\alpha(z)$, gravity $\gamma(z)$, specific heat C_p and mantle potential surface temperature $T_{um,0}$; Section 2.3.1), further parameters determining thermal expansivity ($a_0, a_1, b, \delta_{T0}, \rho_0, \rho$; symbols explained in Section 2.3.2), the product of Clapeyron slope and density jump $\Gamma\Delta\rho$ determining jumps in the adiabatic temperature profile across phase boundaries (Section 2.3.3), and parameters $T_{CMB}, T_0, d_{D''}$ and d_{lith} defining thermal structure of TBLs (Section 2.3.4).

2.3.1 Adiabatic temperature profile

An adiabatic temperature profile can be computed by integration of

$$\frac{d\overline{T}}{dz} = \overline{T}(z) \cdot \alpha(z) \cdot \gamma(z) / C_p(z). \tag{12}$$

Starting point is mantle potential surface temperature (i.e. extrapolation of the mantle adiabat to the surface) $T_{um,0}$. We use $T_{um,0} =$

$1340°C = 1613$ K based on decompression melt studies of MORBs (White & McKenzie 1995; Iwamori *et al.* 1995). The gravity profile $\gamma(z)$ can be computed from the Earth's radial density distribution and is, therefore, known rather accurately. For heat capacity, we adopt $C_p \approx 1250$ J kg^{-1} K^{-1} (e.g. Stacey 1992; Schubert *et al.* 2001), which is also considered to be known rather accurately. Since α also depends on temperature, the radial profiles for α and $\overline{T}$ are determined jointly.

2.3.2 Thermal expansivity

The relation between thermal expansivity and density (along isotherms) can be expressed in the form

$$\left(\frac{\partial \ln \alpha}{\partial \ln \rho}\right)_T = -\delta_T. \tag{13}$$

In the upper mantle, a constant $\delta_T = 5.5$ is used here as reference case. Chopelas & Boehler (1989) experimentally determined $\delta_T = 5.5 \pm 0.5$. In this case, integration yields

$$\alpha(p, T) = \alpha_0(T)\left(\frac{\rho(p, T)}{\rho_0(T)}\right)^{-\delta_T}, \tag{14}$$

whereby $\alpha_0(T)$ and $\rho_0(T)$ are thermal expansivity and density as a function of temperature at zero pressure. Experimental results exist for both $\alpha_0(T)$ and $\rho(p, T)/\rho_0(T)$. We follow here Schmeling *et al.* (2003) where explicit formulae and original references were given. Their treatment is simplified, in that they do not consider the effect of phase transitions. Therefore, we also use the profile derived by Calderwood (1999) for a pyrolite mineral phase assemblage for comparison.

In the lower mantle, depth dependence of δ_T may play a role. The relation between δ_T and ρ was found to be

$$\delta_T = \delta_{T0}\left(\frac{\rho_0(T)}{\rho(p, T)}\right)^b, \tag{15}$$

with $\delta_{T0} \approx 5.5$ and $b \approx 1.4$ (Anderson *et al.* 1992; Schubert *et al.* 2001). In this case, integration along isotherms yields

$$\alpha(p, T) = \alpha_0(T)\exp\left\{-\frac{\delta_{T0}}{b}\left[1 - \left(\frac{\rho_0(T)}{\rho(p, T)}\right)^b\right]\right\}. \tag{16}$$

We will use this equation in the lower mantle in the reference case, however, we will additionally show results with constant $\delta_T = 5.5$ in the entire mantle, in order to assess how large the effect of the depth dependence of δ_T on our results is. We use

$$\alpha_0(T) = (a_0 + a_1 T/1000 \text{ K}) \cdot 10^{-5} \text{ K}^{-1}, \tag{17}$$

with $a_0 = 2.9$ and $a_1 = 0.9$ in the reference case. This is intermediate between various experimental results and *ab initio* calculations for MgSiO$_3$ perovskite, the main lower mantle constituent (Oganov *et al.* 2001). For magnesiowüstite (MgO), another major lower mantle constituent, $\alpha_0(T)$ is probably similar but slightly higher (e.g. Duffy & Anderson 1989, fig. 5). Because of the considerable uncertainty, we consider cases for higher or lower α_0 as well.

Actual density in the lower mantle is reasonably well known, and ρ_0 can, for example, be determined by extending the PREM (Dziewonski & Anderson 1981) lower mantle density profile to the surface. However, the PREM profile is approximately adiabatic, and not isothermal. Hence, the PREM value has to be corrected for adiabatic temperature difference. Transition of the majorite phase, which constitutes about 30 per cent of mantle material, is not abrupt but
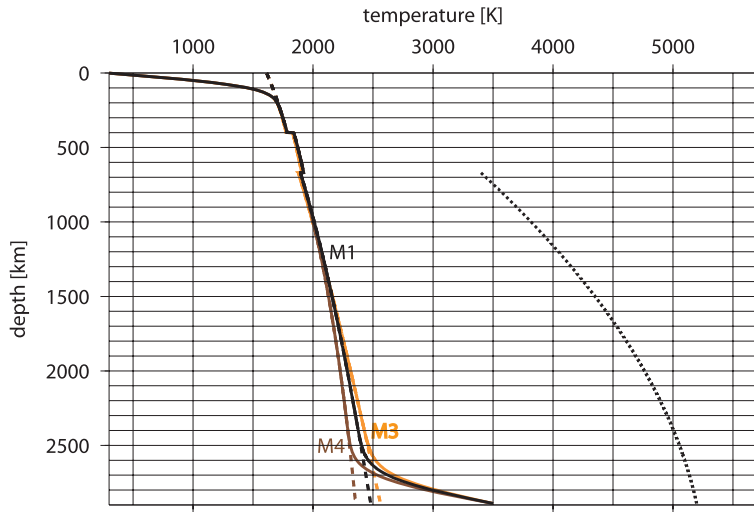
Figure 2. Computed adiabatic temperature profiles (dashed lines), and temperature profiles with thermal boundary layers (solid lines). Black lines: reference case; orange lines: computation using thermal expansivity profile of Calderwood (1999) (see Fig. 3); brown line: computation with constant δ_T, all other assumptions as in reference case. Labels indicate model numbers (Table 2) here and in the following figures. The dotted line shows again the assumed lower mantle melting temperature.

occurs gradually between about 660 and 730 km (e.g. Akaogi & Ito 1999). Therefore, within this depth range, we use a linear superposition $\alpha(z) = \alpha_{lm}(z) + 0.3 \cdot (\alpha_{um}(z) - \alpha_{lm}(z)) \cdot (z - 730 \text{ km})/(660 \text{ km} - 730 \text{ km})$ whereby α_{um} and α_{lm} are determined with eqs (14) and (16), respectively.

2.3.3 Temperature jumps at phase boundaries

Temperature jumps at phase boundaries are smeared out due to diffusion, but the jump between adiabatic profiles above and below phase boundaries is

$$\Delta T_L = Q_L/C_p = \Gamma \Delta \rho T_{pb}/(\rho_{pb}^2 C_p). \quad (18)$$

Hereby is Q_L the latent heat release per unit mass, Γ is the Clapeyron slope, $\Delta \rho$ is the density jump across the phase boundary, T_{pb} is the average temperature below and above the phase boundary, and ρ_{pb} is the average density above and below the phase boundary. Two phase transitions at depths 400 and 660 km are considered here. In the reference case, for depth 400 km, $\Gamma \Delta \rho = 0.5 \cdot 10^3$ MPa K^{-1} · kg m^{-3} is used, based on Akaogi *et al.* (1989) for a pyrolite mantle with 60 per cent olivine content, for depth 660 km, $\Gamma \Delta \rho = -0.3 \cdot 10^3$ MPa K^{-1} · kg m^{-3} is used, as given by Akaogi & Ito (1999). Besides the spinel–perovskite transition, this value also includes the effects of the majorite–perovskite transition, which occurs at a similar depth with positive Clapeyron slope.

2.3.4 Temperatures at the top and bottom of the mantle

At the top and bottom of the mantle are two TBLs with larger temperature gradient. Temperature at the CMB is $T_{\text{CMB}} = 4000 \pm 600$ K according to Boehler (1996) and Schubert *et al.* (2001). The thickness of the TBL is estimated to be about 200 km (Schubert *et al.* 2001), but it may be thicker, if there are chemical variations at the base of the mantle. We use $T_{\text{CMB}} = 3500$ K, bottom TBL thickness $d_{D''} = 200$ km, surface temperature $T_0 = 285$ K and top TBL thickness $d_{\text{lith}} = 100$ km in the reference case. For the difference between adiabatic and actual temperature profile at distance x from

a thermal boundary with total non-adiabatic temperature drop ΔT_0 and thickness d we use $\Delta T = \Delta T_0 \cdot [1 - \text{erf}(x/d)]$.

2.3.5 Temperature and thermal expansivity profiles

Resulting temperature profiles are shown in Fig. 2. The effect of using different thermal expansivity profiles, and of phase boundaries are both rather small.

Corresponding thermal expansivity profiles are shown in Fig. 3. The black 'reference profile' features a decrease from $\approx 2.5 \cdot 10^{-5}$ K^{-1} below 670 km to $\approx 1.0 \cdot 10^{-5}$ K^{-1} at the base of the mantle, in agreement with Schubert *et al.* (2001). For comparison, the profile of Calderwood (1999), derived from a pyrolite mineral phase assemblage and thermal expansivities of individual phases is also shown. It agrees with the reference profile qualitatively, but decreases somewhat less with depth in the lower mantle. Differences
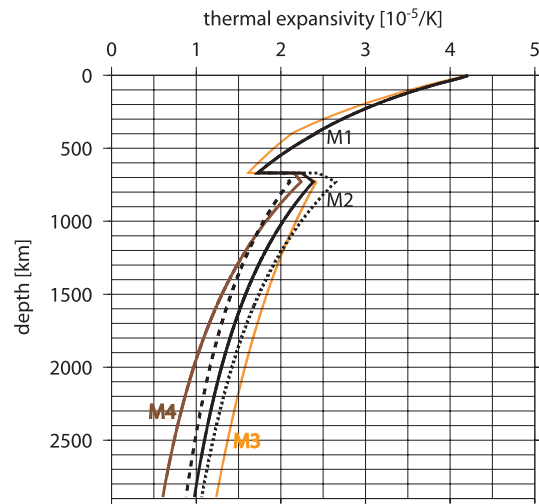
Figure 3. Thermal expansivity profiles for the same cases as shown in Fig. 2. Additionally, the dashed line shows the profile with α_0 reduced by 0.6 · 10^{-5} K^{-1}, the dotted line with α_0 increased by the same amount.

do not exceed $\approx$20 per cent. Thermal expansivity decreases more strongly with depth, if a constant δ_T is assumed. The dashed line is obtained, if $\alpha_0(T) = (2.3 + 0.9\,T/1000\,\mathrm{K}) \cdot 10^{-5}\,\mathrm{K}^{-1}$ is used instead, the dotted line for $\alpha_0(T) = (3.5 + 0.9\,T/1000\,\mathrm{K}) \cdot 10^{-5}\,\mathrm{K}^{-1}$. Both values are still within the range of results proposed (Oganov *et al.* 2001). All profiles show an overall decrease with depth, but an increase with depth across the 660 km discontinuity. Qualitatively, this jump corresponds to α_0 being larger for lower mantle materials than for upper mantle materials (see e.g. Duffy & Anderson 1989, fig. 5).

2.4 Normalized radial viscosity profile—results

We can now express

$$\eta(z) = q_i \cdot \eta_0 \cdot \tilde{\eta}(z). \tag{19}$$

η_0 is a constant scaling viscosity. $\tilde{\eta}(z)$ shown in Fig. 4 is the normalized viscosity profile proportional to $F_{rT}(z)$ from eqs (7) and (11), but adjusted by adding a constant to H in the lower mantle such that the jump in $H(z)/nR$ between upper and lower mantle is removed. This adjustment is of no consequence to the results, and merely serves to make the factors q_i more easily interpretable. Without the adjustment, $\tilde{\eta}(z)$ would increase by a factor $\sim$2000 from above to below 660 km because of the different viscosity law assumed above and below. This jump would be smaller for a lower value of g', and approximately removed for $g' = 8$. Our results will show that such a lower value of g' (corresponding to a less steep profile in the lower mantle) also increases the fit to the geoid. Factors q_i in individual layers (lithosphere, upper mantle, one to two layers transition zone, lower mantle) are treated as free parameters in the optimization discussed below. Figuratively speaking, the optimization consists of shifting corresponding parts of the curves in Fig. 4 to the left or right. $\tilde{\eta}(z)$ is only shown below depth 70 km, because the mechanisms discussed here are not appropriate to model deformation of the lithosphere, and lithospheric viscosity is treated as a free parameter. It is shown for the same three cases as in Fig. 2. All profiles shown
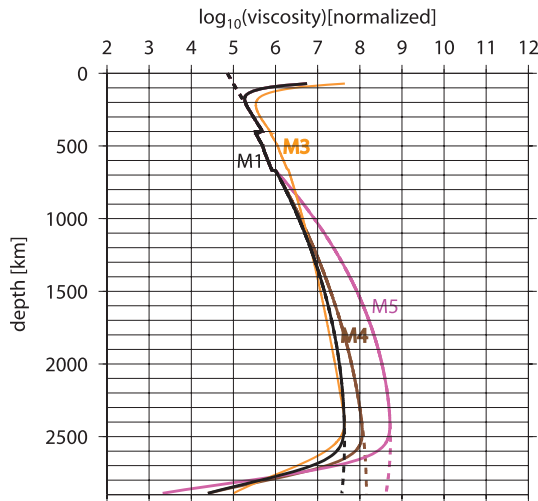
Figure 4. Black and brown lines: non-optimized, normalized viscosity profiles for for the same cases as shown in Fig. 2. Additionally, the violet line shows the profile computed with $g' = 20$ instead, and the orange line shows the profile of Calderwood (1999). Dashed lines are adiabatic profiles, solid lines are with thermal boundary layers. During the optimization, parts of the profiles are shifted left or right relative to each other, yielding optimized profiles as in Figs 9, 13, 14 and 15.

feature a characteristic hump in the lower mantle, like the profiles derived by Ranalli (1995) for whole-mantle flow. The curvature of the hump depends on the curvature of the assumed melting curve. For example, the profile derived by Calderwood (1999) in a similar manner is less curved in most of the lower mantle. The height of this hump strongly depends on the value of g' and also depends on mantle potential surface temperature. Variations in the shape of the $\tilde{\eta}(z)$ profile in the lower mantle as a result of changing potential surface temperature by $\pm$100 K can be closely mimicked by appropriate (small) changes in g' and are, therefore, not considered separately. Whereas in the reference case, the viscosity increase from below 660 km to the maximum in the lower mantle is about a factor 40, it is about a factor 100 for the brown line, although the only difference is a slightly smaller temperature increase towards the base of the mantle, and it is even about a factor 500 for the violet line with $g' = 20$. We, therefore, discuss the effect of g' on our model, and which range of g' gives best results. Additionally, we discuss the effect of $d_{D''}$ and T_{CMB}, corresponding to the thickness of the basal mantle layer where viscosity is decreased, and to the total viscosity decrease, and which combinations of T_{CMB} and $d_{D''}$ yield optimal results. Steinberger & Holme (2006) extend this discussion to include the effect of a basal layer with chemical variations.

2.5 Relation between seismic velocity variations and temperature variations

If variations in seismic *s* wave speed are of thermal origin, they relate to temperature variations through

$$\delta T = (\delta v_s / v_s(z))/(\partial \ln v_s/\partial T)_p. \tag{20}$$

$\delta v_s / v_s(z)$ are relative seismic wave speed variations, for which a number of global tomography models exist. $(\partial \ln v_s/\partial T)_p$ is the partial derivative of the logarithm of seismic *s* wave speed with respect to temperature at constant pressure. Following Karato (1993), it can be written as

$$-\left(\frac{\partial \ln v_s}{\partial T}\right)_p = -\left(\frac{\partial \ln v_{s,0}}{\partial T}\right)_p + F(\alpha) \cdot \frac{Q^{-1}}{\pi} \cdot \frac{H}{RT^2}, \tag{21}$$

whereby the first term is the anharmonic part and the second one the anelastic part. Q is the seismic Q-factor, and we set $F(\alpha) = 1$. With eq. (10) this becomes

$$-\left(\frac{\partial \ln v_s}{\partial T}\right)_p = -\left(\frac{\partial \ln v_{s,0}}{\partial T}\right)_p + F(\alpha) \cdot \frac{Q^{-1}}{\pi} \cdot \frac{gT_m}{T^2}, \tag{22}$$

in the lower mantle.

2.5.1 Anelastic part

We consider two Q profiles here: The first one follows Anderson & Hart (1978) except that a continuous instead of a stepwise profile is used. It is similar in shape to the logarithm of the non-dimensional viscosity profiles $\tilde{\eta}(z)$ in Fig. 4, which makes intuitively sense, since both anelasticity and viscosity are caused by similar mechanisms. Because of this similarity, we use the Anderson & Hart (1978) profile rather than a newer one. For the second profile, we choose the shape to exactly coincide with $\log(\tilde{\eta}(z))$, hence we choose a, b and c such that $Q_2(z) = a + bz + c\log(\tilde{\eta}(z))$ agrees with Anderson & Hart (1978) at depths 250 km, 2400 km and the base of the mantle. Both profiles for the anelastic part are shown in Fig. 5. In the reference case, we use an anelastic part that is the arithmetic average for the two cases described. Q is also expected to depend on temperature, hence
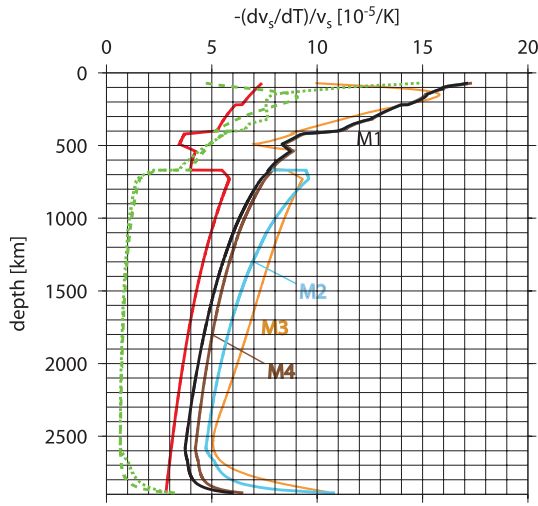
Figure 5. Profiles of $-(\partial \ln v_s / \partial T)_p$, and contributing parts. Red line: anharmonic part. Green lines: anelastic part. The dotted line is for the Q-profile of Anderson & Hart (1978), the dashed line for $Q_2(z)$. Black line: anharmonic plus anelastic part in the reference case (arithmetic average of two green lines). Orange line: profile derived by Calderwood (1999). The blue line uses $g = 30$ for the anelastic part (eq. 22) instead. Brown line: same case as in Figs 2 to 4. Other model assumptions are as in the reference case.

a more accurate treatment should also consider lateral variations of Q, for which models exist, at least in the upper mantle (Gung & Romanowicz 2004).

2.5.2 Anharmonic part

For $(\partial \ln v_{s,0} / \partial T)_p$ we adopt the profile given by Goes *et al.* (2004) in the upper mantle. It is based on values for individual phases and the mantle phase diagram of Ita & Stixrude (1992) for a pyrolite mantle, using a geotherm similar to the reference case geotherm in Fig. 2.

In the lower mantle, $(\partial \ln v_{s,0} / \partial T)_p$ is recomputed to ensure consistency with our profile of $\alpha(z)$. We follow Duffy & Anderson (1989) in assuming that radial derivatives of shear modulus μ for different temperatures are related through

$$\frac{d\mu}{dz}(\overline{T}(z) \pm \Delta T(z)) = \frac{d\mu}{dz}(\overline{T}(z))(1 \pm \alpha(z)\Delta T(z)). \quad (23)$$

This is based on the observation that in the PREM (Dziewonski & Anderson 1981) lower mantle approximately

$$\frac{d \ln \left(\frac{d\mu}{dp} \right)}{d \ln \rho} \approx -1, \quad (24)$$

and the implicit assumption that this also holds along isobars.

$\mu(\overline{T}(z) \pm \Delta T(z))$ is determined by integrating eq. (23) along adiabats, while computing temperature and thermal expansion coefficients along the same adiabats. Starting point is

$$\mu(T_{lm,0} \pm \Delta T_0) = \mu(T_{lm,0}) \pm \Delta T_0 \cdot \frac{d\mu_0}{dT}, \quad (25)$$

at $z = 0$. Based on parameters compiled by Cammarano *et al.* (2003) and the pyrolite phase diagram of Ita & Stixrude (1992) it is estimated $\frac{d\mu_0}{dT} = 27$ MPa K^{-1} for lower mantle mineralogy. $\overline{T}(z)$ and $\alpha(z)$ are computed for the entire mantle with the lower mantle formulation described above. 'Lower mantle potential surface temperature' $T_{lm,0}$ is found iteratively by matching the previously determined lower mantle temperatures. $\frac{d\mu}{dz}(\overline{T}(z))$ and $\mu(T_{lm,0})$ are

determined from the parameters of PREM layer 4, which comprises most of the lower mantle. Thus

$$\left. \frac{\partial \mu}{\partial T} \right|_p \approx \frac{\mu(\overline{T}(z) + \Delta T(z)) - \mu(\overline{T}(z) - \Delta T(z))}{2\Delta T(z)}, \quad (26)$$

is found, and with this $(\partial \ln v_{s,0} / \partial T)_p$ can be computed (Fig. 5).

2.5.3 Sum of anharmonic and anelastic part

For the sum of anharmonic and anelastic part, agreement between our reference case and Calderwood (1999) is good in the upper mantle (Fig. 5), and would be even better if $Q_2(z)$ was used, but our reference profile is lower in the lower mantle: There, we choose the factor $g = 12$ in the relation between activation enthalpy and melting temperature. This value is much lower than previous estimates of $g = 20$–40 (Karato 1993) and thus leads to a smaller anelastic contribution: The blue curve where $g = 30$ is used for computation of the anelastic part (eq. 22) is higher in the lower mantle. The brown curve corresponds to somewhat lower temperatures in the lowermost mantle (see Fig. 2) and is, therefore, also somewhat higher in the lowermost mantle. On the other hand, because of the different way of computation, we compute a larger anharmonic part than Karato (1993) in the lower mantle. In our model, the anharmonic part is larger below 660 km than above 660 km, because of larger values of $\frac{d\mu_0}{dT}$ (Cammarano *et al.* 2003). Differences for anharmonic and anelastic parts between our results and those of Karato (1993) partly compensate each other, such that the sum curve we obtain in our reference model is similar to that of Karato (1993).

2.6 Relation between seismic velocity variations and density variations

The scaling factor $(\partial \ln \rho / \partial \ln v_s)_p$ is then obtained by dividing thermal expansivity through $-(\partial \ln v_s / \partial T)_p$ (Fig. 6). In the reference case, it is similar to Calderwood (1999) in the upper mantle, but, corresponding to differences in Figs 3 and 5 somewhat larger in the lower mantle. Again, the overall shape is similar to that of Karato (1993). For the profiles derived here, the scaling factor somewhat decreases with depth in the lower mantle, whereas the
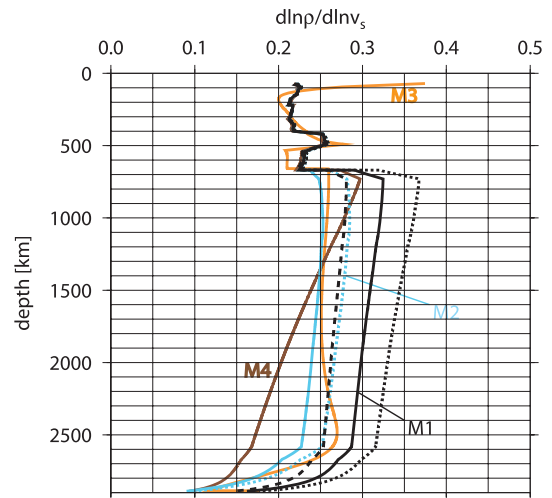
Figure 6. Profiles of scaling factors $(\partial \ln \rho / \partial \ln v_s)_p$ for the same cases as in Figs 3 and 5. Additionally, the dotted blue line is with $a_0 = 3.5$ and $g = 30$.

profile derived by Calderwood (1999) is almost constant over most of the lower mantle, due to a smaller decrease of thermal expansivity with depth. In the case with constant δ_T (brown line), the two effects of stronger decrease of thermal expansivity with depth (Fig. 3) and less decrease of the $-(\partial \ln v_s / \partial T)_p$ profile (Fig. 5) combine to a much stronger decrease of scaling factor with depth. A lower scaling factor in the lower mantle is obtained if either a lower α_0 (black dashed line) or a larger g (blue lines) is assumed. Changing potential surface temperature shifts the scaling factor profile (less than about ± 10 per cent change for ± 100 K potential temperature change), and similar changes would also occur if a different Q-factor profile was used. Because we obtain similar changes also by changing F_l, a_0 and/or g, changes in potential surface temperature and Q-factor profile are not considered separately.

In the reference model, the scaling factor is arbitrarily reduced, compared Fig. 6, by a factor $F_l = 0.5$ in the uppermost 220 km, in order to account for the fact that density variations within the lithosphere are probably only partly of thermal origin. Similarly, other studies set density anomalies at lithospheric depths to zero (Lithgow-Bertelloni & Silver 1998; Becker *et al.* 2003; Behn *et al.* 2004). However, we also consider the effect of varying F_l on our results and discuss which values give best results. In most cases, and unless mentioned otherwise, we use tomography model *smean* (Becker & Boschi 2002) for seismic velocity variations. Other tomography models are also considered.

3 OPTIMIZATION PROCEDURE

3.1 Mantle flow computation

We can now combine a scaling factor profile as derived in the previous section with an *s*-wave tomography model to obtain a density model. With a viscosity profile as described above, mantle flow can be computed. Equations of viscous flow are solved with a spectral method originally developed by Hager & O'Connell (1979, 1981): Only radial viscosity variations are considered, thus the equations decouple in the spherical harmonic domain and can be solved separately for each spherical harmonic. In the reference case, and if not mentioned otherwise, spherical harmonic expansion is done up to $l_{\max} = 15$, but cases with $l_{\max} = 31$ are considered as well. The original method was modified to consider depth-dependent gravity (from PREM), and to include the effects of compressibility (as described in Steinberger 2000, following Panasyuk *et al.* 1996), and of deflections δz of phase boundaries at depth 400 and 660 km in thermal equilibrium. The latter effect was included as sheet mass anomalies

$$\delta z \cdot \Delta \rho = \frac{\Gamma \Delta \rho}{\rho_{pb}^2 \gamma_{pb} \alpha_{pb}} \cdot \delta \rho, \tag{27}$$

whereby $\delta \rho$ is the density anomaly as inferred from the tomography model, at the depth of the phase transition. ρ_{pb}, γ_{pb} and α_{pb} are density, gravity and thermal expansivity at the phase boundary. Values for $\Gamma \Delta \rho$ were given in the previous chapter. For ρ_{pb}, the average value between above and below the phase boundary (from the PREM model) is used, for α_{pb}, we use $2.079 \cdot 10^{-5}$ K^{-1} at 660 km and $2.378 \cdot 10^{-5}$ K^{-1} at 400 km—approximate average values between above and below the phase boundary from the reference case in the previous chapter.

3.2 Variables in optimization

The optimization consists of finding the minimum of a misfit function in parameter space. Parameter space consists of the viscosity factors q_i, $i = 1 \ldots n_{\mathrm{vis}}$ in eq. (19). n_{vis} is the number of layers where viscosity is considered to vary independently. In most cases, we use $n_{\mathrm{vis}} = 4$, in which case $i = 1$ corresponds to the lithosphere (0–100 km), $i = 2$ the upper mantle (100–400 km), $i = 3$ the transition zone (400–660 km) and $i = 4$ the lower mantle (below 660 km). In some cases, the upper part of the transition zone (400–520 km) and its lower part are considered separately. In this case, it is $n_{\mathrm{vis}} = 5$, $i = 3$ corresponds to the upper part of the transition zone, $i = 4$ its lower part and $i = 5$ the lower mantle. Besides these parameters allowed to vary within each optimization, variations are also considered for a number of further parameters. These are kept constant within each optimization, and the optimization is performed for several sets of parameter values, and several 2-D grids in parameter space. These further parameters include a_0, b, g, g', T_{CMB}, $d_{\mathrm{D''}}$ and F_l (see Table 1).

3.3 Haskell constraint

The Haskell constraint states that the logarithmic average of viscosity, weighted with an appropriate sensitivity kernel equals about 10^{21} Pa s. We express it in the form

$$\int_{120\,\mathrm{km}}^{\mathrm{CMB}} \log_{10} \left(\frac{\eta(r)}{1\,\mathrm{Pa\,s}} \right) \cdot K(r)\, dr \Big/ \int_{120\,\mathrm{km}}^{\mathrm{CMB}} K(r)\, dr = 21, \tag{28}$$

and use the sensitivity kernel for the Angerman River site given by Mitrovica (1996) for $K(r)$ (Fig. 7). If we choose η_0 such that, in eq. (19) $\eta_0 \cdot \tilde{\eta}(z)$ satisfies the Haskell constraint, we find that $\eta(z)$ also does if $1.67 \cdot q_2 + 1.33 \cdot q_3 + q_4 \approx 0$ in the case of one transition zone layer, and $1.67 \cdot q_2 + 0.67 \cdot q_3 + 0.66 \cdot q_4 + q_5 \approx 0$ in the case of two. We, therefore, choose the penalty function

$$P_1 = (1.67 \cdot q_2 + 1.33 \cdot q_3 + q_4)^2, \tag{29}$$

in the first case, and a corresponding function in the second.
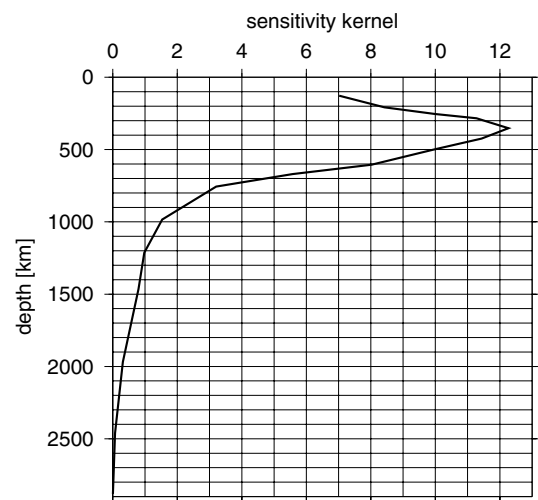
Figure 7. Kernel showing the sensitivity of post-glacial rebound to viscosity at various depths. From Mitrovica (1996) for Angerman River.

3.4 Heat flux constraint

For each density field and corresponding flow field, the advected heat flux is computed by integrating radial velocity v_r times heat anomaly $\delta T \cdot C_p \cdot \rho = \delta \ln v_s / (\partial \ln v_s / \partial T)_p \cdot C_p \cdot \rho$ over spherical surfaces at given depths:

$$\Phi(r) = C_p \cdot \rho / (\partial \ln v_s / \partial T)_p \cdot \int_S \delta \ln v_s \cdot v_r dA. \qquad (30)$$

For this computation present-day surface plate motions (DeMets *et al.* 1990) are used as boundary condition. This curve should approximately fall between theoretical steady-state profiles for an internally heated mantle and a basally heated mantle. Here we implement this constraint by penalizing if $\Phi(r) > \Phi_{bh}$ or $\Phi(r) < \Phi_{ih}(r)$. For Φ_{bh} we use a constant value 33 TW representing our estimate for the mantle heat flux (Calderwood 1999), which is global heat flux minus heat produced in the crust. Pollack *et al.* (1993) compute a global heat flux 44 TW. By subtracting estimated heat production in the continental crust from it, Schubert *et al.* (2001) estimate a mantle heat flux 37 TW. More recently, Hofmeister (2005) computed a smaller global heat flux 31 ± 1 TW, corresponding to only about 24 TW mantle heat flux. However, another recent analysis (Wei & Sandwell 2006) yielded 42–44 TW. $\Phi_{ih}(r)$ has been modified from the theoretical steady-state profile for an internally heated mantle with constant heat production rate per unit mass in order to account for the fact that conduction is the dominant heat transport mechanism close to the surface (see Fig. 8). We use the penalty function

$$P_2 = \int \frac{\max\left(\frac{\Phi(r)-\Phi_{bh}}{\Phi_{bh}}, 0\right)^2 + \max\left(\frac{\Phi_{ih}(r)-\Phi(r)}{\Phi_{bh}}, 0\right)^2}{2891 \text{ km}} \, dr. \qquad (31)$$

Obviously, the assumption that heat flux at any depth does not change with time, which is implicitly made here, is not exactly satisfied for the Earth. $\Phi(r)$ is time variable and the present-day surface heat flux may be anomalously high or low. Hence we do not require $P_2 = 0$ exactly.

3.5 Geoid constraint

For each density field and corresponding flow field, the inferred geoid is computed; flow deforms boundaries, and both the density anomalies that drive flow and the deformed boundaries contribute to the geoid. The inferred geoid is, therefore, quite sensitive to the assumed viscosity structure. The fit between computed and actual geoid is expressed in terms of the penalty function

$$P_3 = \frac{\text{Var(Predicted–Observed)}}{\text{Var(Observed)}}. \qquad (32)$$

$1 - P_3$ is referred to as (geoid) variance reduction. For the geoid computation, stress-free boundaries at the Earth's surface and CMB are assumed in the reference case; however, other boundary conditions at the Earth's surface are considered as well.

3.6 Misfit function

We optimize the model in parameter space by minimizing a misfit function using a downhill simplex method (Press *et al.* 1986). This method finds a local, not necessarily global minimum in parameter space. In most cases, we will either minimize

$$\Pi_1 = c_1 \cdot P_1 + c_2 \cdot P_2 + P_3, \qquad (33)$$

(misfit criterion 1) or require the Haskell constraint to be fit exactly, and minimize

$$\Pi_2 = c_2 \cdot P_2 + P_3, \qquad (34)$$

under the additional constraint $P_1 = 0$ (misfit criterion 2, corresponding to criterion 1 with $c_1 \longrightarrow \infty$). Cases indicated with a star in Table 2 use criterion 2 (except for M17, M17b in Section 4.9 which use a modified criterion), all others (including those in Figs 11 and 12, but except for cases M19 and M19b in Table 1 and Section 4.2) use criterion 1. In most cases, we will use $c_1 = 1$, $c_2 = 4$. We find that results remain very similar with both criteria, and hence do not strongly depend on c_1, as the Haskell constraint is always fit very well. The value for c_2 is discussed in the next section.
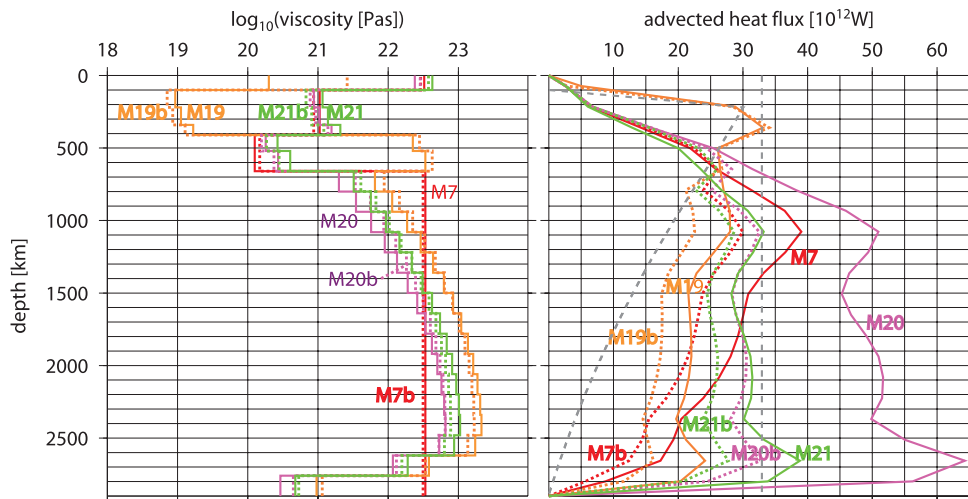
Figure 8. Optimized viscosity profiles (left) and advected heat flux profiles (right), for cases where not all constraints are imposed. Orange lines: only heat flux and Haskell constraint. Violet lines: only geoid and Haskell constraint. Green lines: only geoid and heat flux constraint. Red lines: viscosity profile not based on mineral physics but constant in lithosphere, upper mantle, transition zone and lower mantle. Continuous lines are with parameters as in the reference case, dotted lines as in model 2. Φ_{bh} and $\Phi_{ih}(r)$ are shown as grey dashed lines. The heat flux profiles should approximately lie in between.

Table 2. List of numerical models. The 'comments' column indicates differences to the reference model, except for 'b' models, where it indicates the difference to models without 'b'. VR is geoid variance reduction, P_2 heat flow misfit (eq. 31). Numbers in brackets indicate either results with expansion up to $l_{max} = 31$ (M1–M3b), or with model 2 parameters (M7–21). Stars indicate cases where an exact fit to the Haskell constraint has been prescribed. UM-upper mantle, TZ-transition zone, LM-lower Mantle.

| Model #	comment	VR [per cent]	P_2
M1*	Reference case	75.9 (74.7)	0.0165 (0.0133)
M1b*	Lowest viscosity in asthenosphere	71.6 (70.5)	0.0125 (0.0090)
M2*	$a_0 = 3.5$, $g = 30$	79.7 (78.6)	0.0133 (0.0099)
M2b	Lowest viscosity in asthenosphere	76.0 (75.4)	0.0109 (0.0078)
M3*	Based on Calderwood (1999)	79.5 (78.5)	0.0122 (0.0093)
M3b	Lowest viscosity in asthenosphere	75.3 (74.6)	0.0105 (0.0076)
M4*	$\delta_T = 5.5$ constant	65.7	0.0044
M4b*	Lowest viscosity in transition zone	52.8	0.0140
M5*	$g' = 20$	−15.5	0.0356
M6*	$\eta = $ const in UM, TZ; model 2 parameters	79.6	0.0138
M7 (M7b)	$\eta = $ const in UM, TZ, LM	81.2 (80.8)	0.0163 (0.0143)
M8* (M8b*)	Independent η in upper, lower TZ	80.0 (79.7)	0.0164 (0.0131)
M9* (M9b*)	Tomography model S20RTS	74.2 (76.1)	0.0129 (0.0114)
M10* (M10b*)	Tomography model SB4L18	47.9 (64.6)	0.0175 (0.0052)
M11* (M11b*)	Tomography model Grand (2002)	67.7 (69.0)	0.0250 (0.0296)
M12* (M12b*)	Tomography model SAW24B16	64.7 (74.3)	0.0187 (0.0154)
M13* (M13b*)	Tomography model S12WM13	44.3 (56.0)	0.0188 (0.0086)
M14* (M14b*)	Tomography model S362D1	55.9 (69.3)	0.0116 (0.0066)
M15* (M15b*)	Fixed surface	38.4 (45.8)	0.0138 (0.0194)
M16 (M16b)	Plates moving half free speed	11.2 (19.1)	0.0082 (0.0052)
M17* (M17b*)	Plates free speed, tractions at surface, v_{rms} penalty	24.1 (31.0)	0.0068 (0.0130)
M18* (M18b)	Prescribed plate motions	13.9 (14.8)	0.0029 (0.0034)
M19 (M19b)	Only heat flux and Haskell constraint	−3140.3 (−1923.6)	0.0000 (0.0001)
M20* (M20b*)	Only geoid and Haskell constraint	78.0 (79.7)	0.1133 (0.0134)
M21 (M21b)	Only geoid and heat flux constraint	78.0 (79.5)	0.0173 (0.0138)

4 RESULTS

4.1 Overview

We first show optimized viscosity and heat flux profiles (Fig. 8), as well as variance reduction and heat flow misfit P_2 for cases where the constraints are not all imposed simultaneously (M7, 7b, 19–21b in Table 2). This includes one case with constant viscosities in different mantle layers instead of profiles based on mineral physics. We then go on to imposing all constraints simultaneously and show

results for our reference model (M1; Figs 9 and 10), further 'preferred' models (M2 with $a_0 = 3.5$ and $g = 30$, and M3 with profiles from Calderwood (1999)) and further models (M4, M4b and M5) with stronger depth dependence of either lower mantle viscosity or thermal expansivity (Fig. 9). We then systematically vary parameters a_0, g, g', $n = g/g'$, T_{CMB}, $d_{D''}$ and F_l within bounds as listed in Table 1, and present contour plots of optimized variance reduction (Fig. 11) and heat flow misfit P_2 (Fig. 12) as a function of two of these parameters. Subsequently, we consider results with
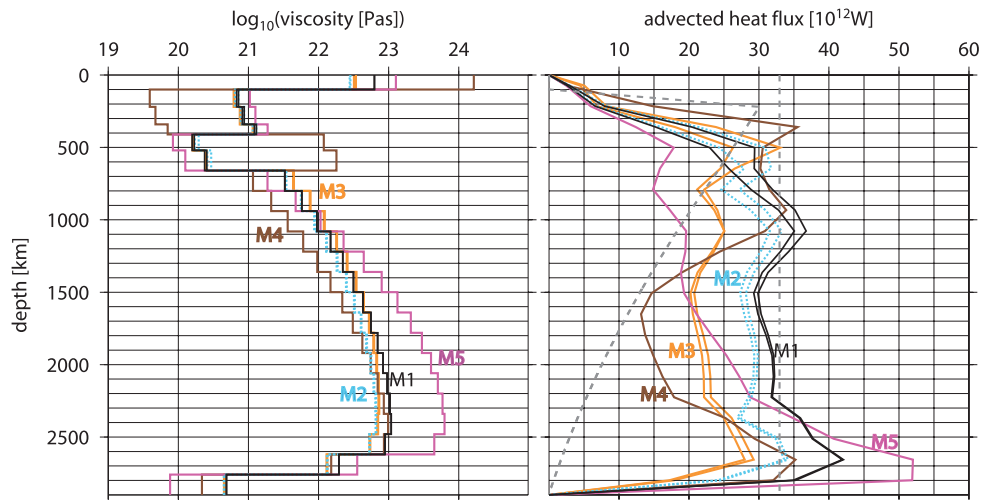
Figure 9. Optimized viscosity profiles (left) and advected heat flux profiles (right). Colour and type of lines correspond to Figs 4 and 6. Φ_{bh} and $\Phi_{ih}(r)$ are shown as grey dashed lines. Per diagram there are two black, orange and blue lines: one, with higher heat flux values in the upper mantle, was computed with $l_{max} = 31$, the other with $l_{max} = 15$.
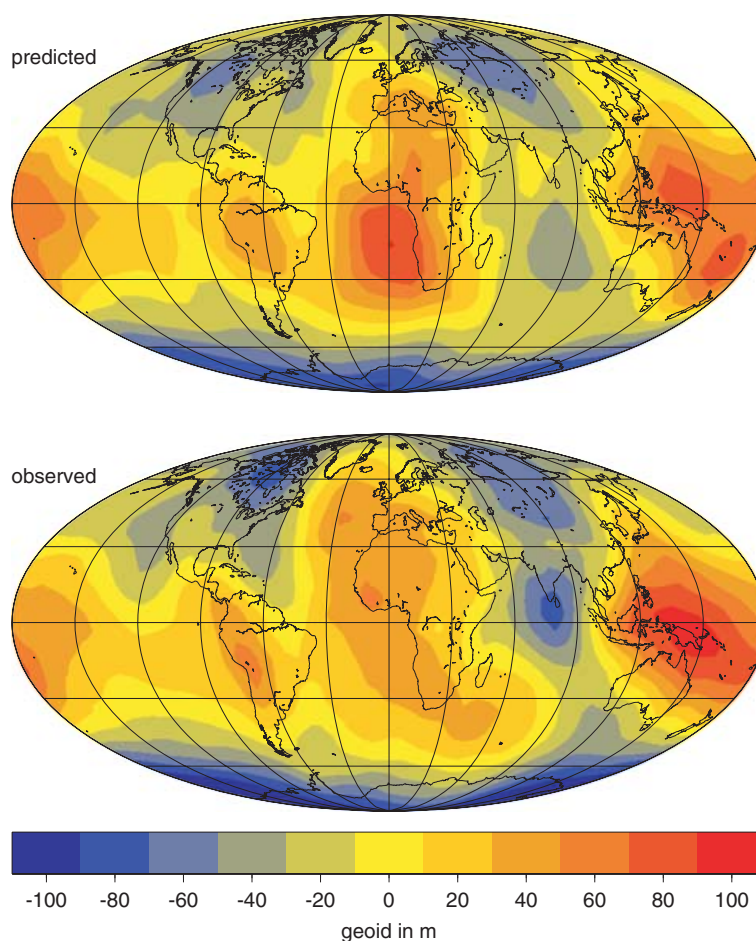
Figure 10. Above: geoid computed for the reference case. below: observed geoid.

the further constraint that viscosity is lowest in the asthenosphere (M1b, M2b, M3b), with constant viscosity in the upper mantle and transition zone (M6) viscosity in the upper and lower part of the transition zone varying independently (M8, 8b) (all in Fig. 13), different tomography models (M9–14b; Fig. 14), and different surface boundary conditions (M15–18b; Fig. 15).

### 4.2 Cases where not all constraints are imposed simultaneously

Discussing model cases where not all constraints have been imposed helps clarifying which features of the results are due to which constraints. Since the geoid fit is only affected by relative viscosity variations, we need at least one additional constraint for the absolute viscosity level—either the Haskell or the heat flux constraint. If we impose geoid and Haskell constraint (use misfit criterion 2 with $c_2 = 0$) we obtain a geoid variance reduction of 78 per cent or 80 per cent with other assumptions as in the reference case (M20) or in case M2 (M20b). Resulting viscosity structure (violet lines in Fig. 8, left-hand side panel) is very similar in both cases. For M20, the computed heat flux is too large in the lower mantle (continuous violet line in Fig. 8, right-hand side panel), whereas for M20b (dotted violet line) it matches the observation-based estimate of mantle heat flux quite well, even without imposing any heat flux constraint. If we impose instead geoid and heat flux constraint (use misfit criterion 1 with $c_1 = 0$ and $c_2 = 4$), we obtain heat flux profiles (green lines in Fig. 8, right-hand side panel) similar to M20b. The optimized viscosity structure in case M21b (dotted green line in Fig. 8,

left-hand side panel) remains very similar to case M20b, that is, the Haskell constraint is matched well in M21b even without imposing it. In case M21 (continuous green line), viscosity is somewhat higher than in case M20 by approximately a factor 1.6 throughout the mantle. Geoid variance reduction (78 per cent in M21 and 79 per cent in M21b) remains similar to cases M20 and M20b, hence with this relative weighting of geoid and heat flux constraint ($c_2 = 4$) the latter is not overly constraining.

We find that both Haskell and heat flux constraint can be simultaneously fit almost perfectly (M19 and M19b); therefore, there is no benefit in looking at cases with only one of them imposed. Resulting viscosity and heat flux profiles if we impose Haskell and heat flux constraint (i.e. minimize Π_1 in eq. (33) with $c_1 = 1$, $c_2 = 4$, and without the term P_3) are shown as continuous (M19) and dotted (M19b) orange lines in Fig. 8. However, there is a huge misfit between predicted and observed geoid. Thus, the geoid constraint is the most essential one.

Finally, with constant viscosities in upper mantle, transition zone and lower mantle we are able to obtain geoid variance reduction 81 per cent and reasonable heat flux profiles (cases M7 and M7b), with lower mantle viscosity of about $3 \cdot 10^{22}$ Pa s. This is similar to results obtained in previous work. The main objective of this paper is to find out whether we can replace the assumption of layers with constant viscosities (in particular in the lower mantle) with viscosity profiles based on mineral physics without substantially degrading the fit to the geoid, heat flux and Haskell constraints.
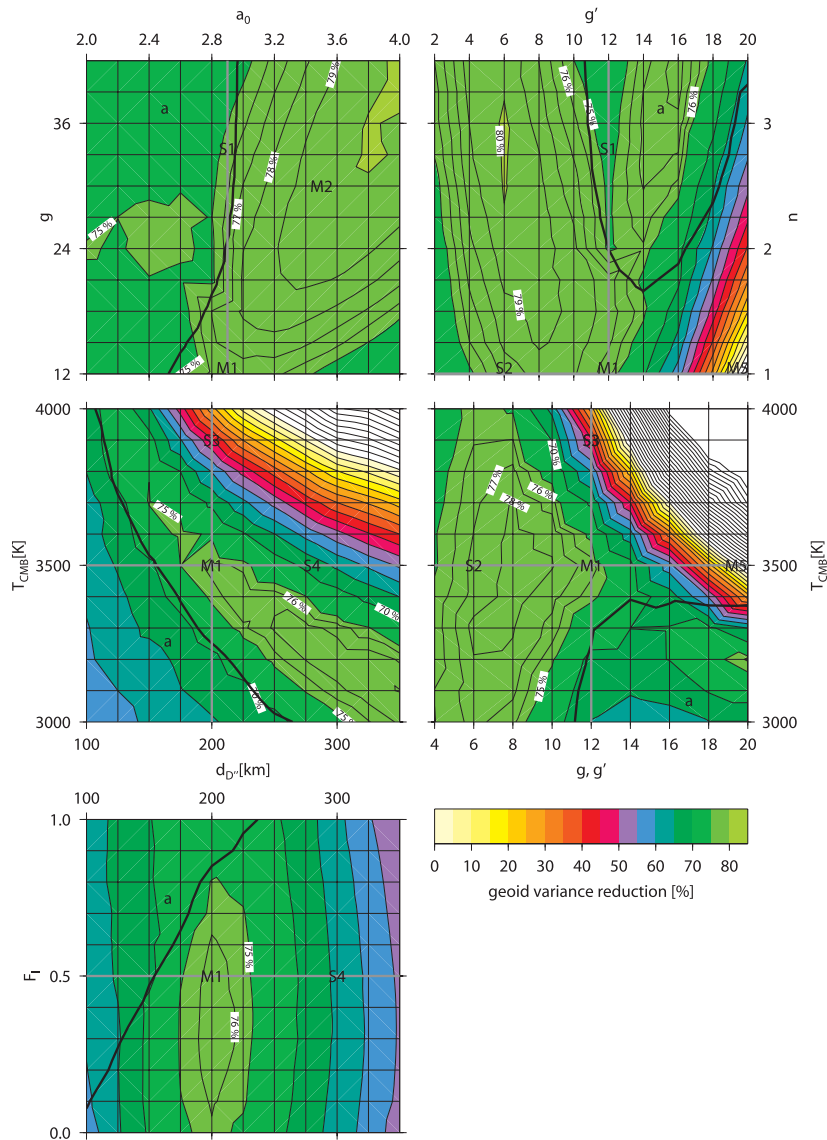
Figure 11. Geoid variance reduction as a function of a_0 and g (but $g' = 12$ constant) (top left), of g' and $n = g/g'$ (top right), of $g = g'$ and T_{CMB} (centre right), of $d_{D''}$ and T_{CMB} (centre left), and of $d_{D''}$ and F_l (bottom left); other parameters as in the reference case. These are cross-sections through a 5-D parameter space intersecting along the grey lines S1, S2, S3 and S4. For each point, the model has been optimized by minimizing the misfit function $P_1 + 4P_2 + P_3$ in a 4-D parameter space. The thick black line divides regions where the lowest viscosity occurs in the transition zone from where it occurs in the asthenosphere (indicated by the letter 'a'). Location of models M1, M2 and M5 is also indicated.

4.3 Reference case

Fig. 10 compares the predicted geoid with the observed one in the reference case (M1). The variance reduction is 76 per cent. This is slightly less than in cases M20 and M21 above—as more constraints are imposed simultaneously, the fit to the geoid is somewhat reduced. The optimized viscosity model and corresponding advected heat flux profiles for cases given in Figs 4 and 6 are shown in Fig. 9; for the reference case (black lines), the difference between the lowest viscosity (in the transition zone) and the highest viscosity at the base of the mantle is about a factor 700. With the relative weighting of geoid and heat flux constraint $c_2 = 4$ variance reduction decreases by only a few per cent compared to the case without any heat flux constraint. At the same time the heat flux constraint is probably fit well enough considering possible time variations in heat flux mentioned above. We will hence maintain this relative weighting in what follows.

4.4 Dependence on thermal expansivity and relation between *s* wave speed and temperature

We can achieve an even higher variance reduction with a somewhat higher α and larger g in eq. (22) while keeping $g' = 12$ in the viscosity law eq. (11), resulting in higher values of $-(\partial \ln v_s/\partial T)_p$ and lower values of $(\partial \ln \rho/\partial \ln v_s)_p$. For example, the model with $a_0 = 3.5$ and $g = 30$ (M2; blue dotted lines) gives a variance reduction of 80 per cent. Also, the heat flux profile now fits even better, as it stays below 34 TW throughout the mantle. We saw above for cases M20b and M21b that with these parameters a good fit to the heat flux or Haskell constraint is obtained even without applying those constraints. Hence it is not surprising that results stay very similar if, in case M2, we apply these constraints simultaneously.

Also, if both profiles for thermal expansivity and $-(\partial \ln v_s/\partial T)_p$ are adopted from Calderwood (1999), a variance reduction of 80 per cent is achieved along with a suitable heat flux profile
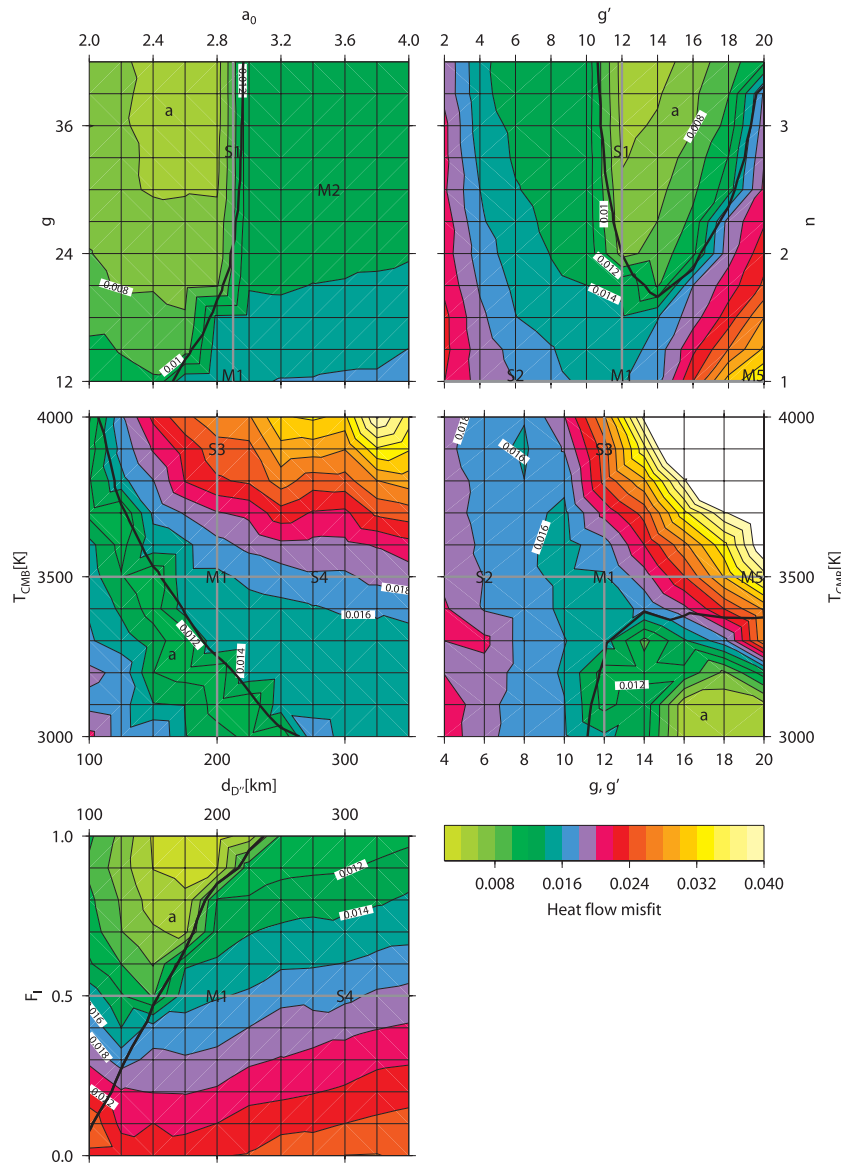
Figure 12. Misfit P_2, as defined in eq. (31), of the heat flux profile for the same cross-sections and models as in Fig. 11, where further explanations are given.

(M3; orange lines). However, heat flux in the uppermost few 100 km below the lithosphere is under-predicted in all three models discussed so far—and this is in fact a general problem with all models that give otherwise a good fit. Likely explanations for this misfit are discussed in the last section. This misfit is somewhat less with $l_{max} = 31$. In this case geoid variance reduction is slightly reduced to 75, 79 and 78 per cent, respectively, for the three cases M1, M2 and M3 considered thus far.

The dependence of variance reduction and misfit function on g used in the velocity-temperature relation eq. (22) and a_0, but keeping $g' = 12$ in the viscosity law eq. (11) is further illustrated in the top left panels of Figs 11 and 12: If a_0 and g are both increased relative to the reference case $g = 12$, both geoid variance reduction and the heat flux profile are somewhat improved. For $g = 12$ the highest variance reduction is obtained with somewhat smaller $a_0 \approx 3$ whereas for $g = 42$ it is obtained with somewhat larger $a_0 \approx 4$; both combinations yield values of $(\partial \ln \rho / \partial \ln v_s)_p \approx 0.3$ in the lower mantle, which appears to work best for achieving a good fit to the geoid.

The better fit of the heat flux profile for larger g is a result of the higher values of $-(\partial \ln v_s / \partial T)_p$ in the lower mantle, resulting in lower temperature anomalies inferred from seismic tomography, thus lower inferred heat flux. Probably the improved variance reduction for larger g is due to the same reason; once the heat flux constraint becomes less difficult to satisfy, the optimization can rather focus on optimizing the fit to the geoid.

In the case of a stronger decrease of α with depth (no depth dependence of δ_T, that is, $b = 0$; M4; brown lines in Fig. 9) variance reduction is reduced to 66 per cent. Both the resulting optimum viscosity structure with a rather high transition zone viscosity and heat flux profile look somewhat unrealistic. If, in this case, the lowest viscosity is restricted to occur in the transition zone, profiles look more realistic, but variance reduction in this case (M4b) is further reduced to 52 per cent. Thus, the smaller decrease of α with depth in the reference case appears more appropriate to achieve good results. This is probably partly due to the fact that a constant δ_T leads to less temperature increase with depth, hence a steeper viscosity profile.

4.5 Dependence on lower mantle viscosity

A steeper viscosity profile is also obtained with a larger value of g'. With $g' = 20$ (M5; violet lines in Fig. 9), we obtained a variance reduction of only -15 per cent and the heat flux profile also looks unrealistic. The dependence of variance reduction and heat flux misfit on the steepness of the viscosity profile is further illustrated in the centre right panels of Figs 11 and 12: The viscosity increase through the lower mantle becomes larger with increasing g', the viscosity drop at the base of the mantle becomes larger with increasing T_{CMB}. An increase of either of them relative to the reference case leads to substantial deterioration of both the predicted geoid and heat flux profile, but decrease does not yield substantial improvement. In fact, low values of g tend to also give a larger misfit of the heat flow profile; this arises, as the viscosity hump in the lower mantle is then less high, and thus the heat flux predicted tends to be too high in part of the lower mantle.

The top right panels of Figs 11 and 12 show that the deteriorating fit with increasing g and g' in the centre right panels is in fact due to the viscosity profile; if we leave g' constant in the viscosity relation eq. (11) but increase $g = g'n$ in eq. (22) through increasing n, the fit rather tends to improve—for reasons already discussed for the top left panels.

There is also a trade-off between the assumed temperature at the base of the mantle and the thickness of the thermal boundary layer $d_{D''}$ at its base, as shown in the centre left panels of Figs 11 and 12: For $d_{D''} \approx 350$ km, the highest geoid variance reduction is obtained with $T_{CMB} \approx 3000$ K, for $d_{D''} \approx 200$ km with $T_{CMB} \approx 3500$ K (reference case), and for $d_{D''} \approx 125$ km with $T_{CMB} \approx 4000$ K. The smallest heat flow misfit tends to occur with somewhat smaller thermal boundary layer thicknesses and/or CMB temperatures, as this gives smaller predicted heat flux in the lowermost mantle, which is too high in the reference model.

## 4.6 Dependence on upper mantle velocity to density scaling

In the reference model, the scaling factor is arbitrarily reduced by a factor $F_l = 0.5$ in the uppermost 220 km, in order to account for the fact that density variations within the lithosphere are probably only partly of thermal origin. The bottom left panel of Fig. 11 shows that this is in fact an appropriate choice; the highest variance reduction occurs for intermediate values of F_l around 0.5, but the fit to the geoid does not strongly depend on F_l. On the other hand, the bottom left panel of Fig. 12 shows that a better fit to the heat flow profile is obtained with larger F_l, because this increases the computed heat flow below the lithosphere, thus reducing the misfit there, particularly in cases where the lowest viscosity occurs in the asthenosphere.

4.7 Dependence on upper mantle and transition zone viscosity

The resulting optimized viscosity structure remains very similar in all three cases included in Fig. 9 that give good results—the reference case, model 2 and the case with profiles from Calderwood (1999); it shows a pronounced viscosity decrease in the transition zone—about one order of magnitude relative to above or below.

In order to assess whether the result that the lowest viscosity in our reference model occurs in the transition zone is of significance, we also include an optimization restricted to models with transition zone viscosities higher than in the upper mantle. The variance reduction is then slightly reduced to 72 per cent (71 per cent) with reference case parameters (M1b), 76 per cent (75 per cent) with model 2 parameters (M2b), and 75 per cent (75 per cent) with the profiles from Calderwood (1999) (M3b) (numbers in brackets with $l_{max} = 31$). The heat flux profile remains very similar, and the viscosity maximum in the lower mantle remains similar at about, or slightly below 10^{23} Pa s for all three models (Fig. 13). We find a general tendency that models with lowest viscosity in the transition zone tend to yield somewhat higher variance reduction than models with the lowest viscosity in the asthenosphere (Fig. 11). It is hard to judge whether this slightly reduced variance reduction warrants attaching significance to the result that the lowest viscosity occurs in the transition zone. The best fit of the heat flux profile is obtained for cases where the lowest viscosity occurs in the asthenosphere, since this allows for a higher heat flux in the uppermost few 100 km below the lithosphere, thus reducing the misfit there (Fig. 12).
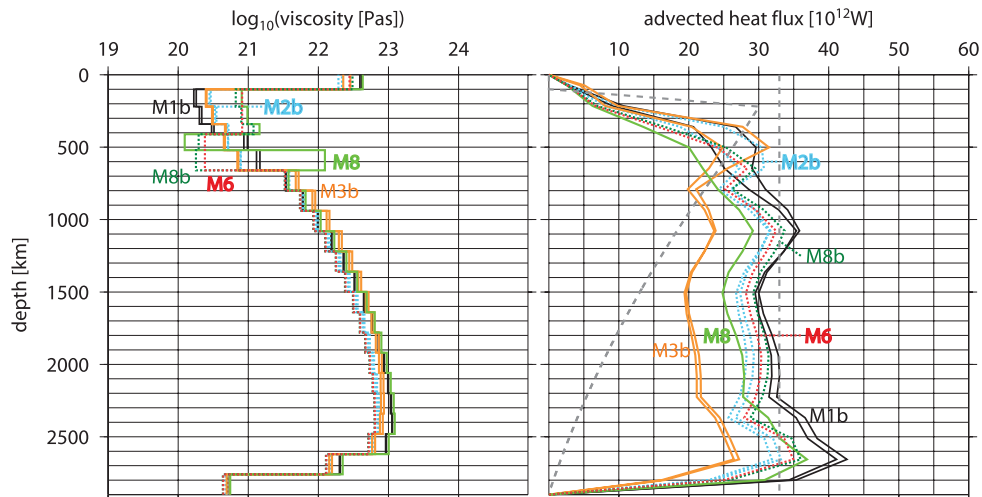
Figure 13. Optimized viscosity profiles (left) and heat flux profiles (right). Black, orange and dotted blue lines (two per diagram) correspond to Figs 9, but with the restriction that lowest viscosities are to occur in the asthenosphere. Light green and dark green dotted lines are for the same models as black and blue dotted lines, but with viscosities in the upper and lower transition zone independently varying. Φ_{bh} and $\Phi_{ih}(r)$ are shown as grey dashed lines. Red dotted lines are for the same case as blue dotted, but with constant viscosities 100–410 and 410–660 km.

Results stay very similar, if the viscosity is kept constant in the upper mantle, and constant in the transition zone (Fig. 13, red dotted lines). This confirms that results—as stated in Section 2.2.2—do not strongly depend on the activation enthalpy profile in the upper mantle. Furthermore, we consider the case that viscosity in the upper and lower part of the transition zone, that is, above/below 520 km, varies independently; in the reference case, this leads to an increase in variance reduction to 80 per cent, with a rather strong viscosity contrast between the upper and lower part of the transition zone. In model 2, variance reduction remains 80 per cent, and the optimized viscosity structure remains very similar. We, therefore, regard the constraints of our method as insufficient to resolve details of the viscosity structure such as the difference between the upper and lower part of the transition zone. We also computed results without consideration of phase boundaries, for an incompressible mantle, and for the two different Q profiles; in all cases results stay very similar, and are therefore not shown.

4.8 Dependence on tomography model

Fig. 14 shows results for different tomography models with model 2 parameters. In most cases, the smallest misfit occurs with the lowest viscosity in the transition zone, only for SB4L18 (M10b) the smallest misfit occurs with the lowest viscosity in the asthenosphere. With reference case parameters, this happens with SB4L18 (M10), Grand's model (M11), SAW24B16 (M12) and S362D1 (M14). The resulting maximum viscosity in the lower mantle is very similar for all models—around, or slightly below 10^{23} Pa s. There are quite large differences between the heat flux profiles for various models. Largely these are due to the differences in rms amplitudes versus depth among the tomography models. For example, Grand's model (blue lines) has higher rms amplitudes than S20RTS (red line) in the lowermost mantle, but lower amplitudes between ≈1500 and 300 km depth. The model smean (black) is an average of Grand's model (blue), S20RTS (red) and SB4L18 (green) and gives a heat flux profile that is approximately constant through much of the mantle. Geoid variance reductions and heat flow misfit P_2 of optimized models are listed in Table 2. There is a general tendency for better

fit with model 2 parameters, which gives smaller density anomalies. In particular, the difference is pronounced for those models with comparatively large amplitudes away from the boundaries, that is, where geoid kernels are larger—such as SB4L18. Such models give generally lower variance reduction, as they would presumably require even lower conversion factors from seismic velocity to density anomalies in order to yield a good fit. Models with lower amplitudes (S20RTS, Grand) tend to give better fit and the difference between the fits with reference case parameters and model 2 parameters is smaller. However, with no individual tomography model were we able to exceed the variance reductions obtained with the average model smean.

4.9 Dependence on upper boundary condition

Upper boundary condition for the computation of the geoid in the models discussed thus far was a free surface. Since this is not entirely appropriate for a surface broken into plates not well characterized by viscous rheology, we show in Fig. 15 results for different surface boundary conditions. For fixed surface, variance reduction of the optimized models with reference case parameters (M15, grey lines) is 38 per cent, with model 2 parameters (M15b, black lines) it is 46 per cent. With plates moving freely according to the forces acting on them due to mantle flow, with tractions applied at the base of the plates at depth 100 km (see Steinberger *et al.* 2001, for a detailed description of the methodology) we obtain a negative variance reduction—also plates are moving too fast compared to observations. Thus, we go on to a case with plates moving at half the speed of free plate motions. In this case (M16, green lines with reference case parameters; M16b, red lines with model 2 parameters), calculated rms plate motions $v_{rms,c}$ are 5.2 cm yr^{-1} (M16) and 5.3 cm yr^{-1} (M16b), similar to the observed $v_{rms,o} = 4.4$ cm yr^{-1}. For the difference between predicted and observed plate motions, rms values are 3.8 cm yr^{-1} in both cases, corresponding to plate motion variance reductions of 25 per cent (M16) and 23 per cent (M16b). Geoid variance reduction remains low at 11 per cent (M16) and 19 per cent (M16b). A similar geoid variance reduction is obtained with prescribed plate motions (13.9 per cent and
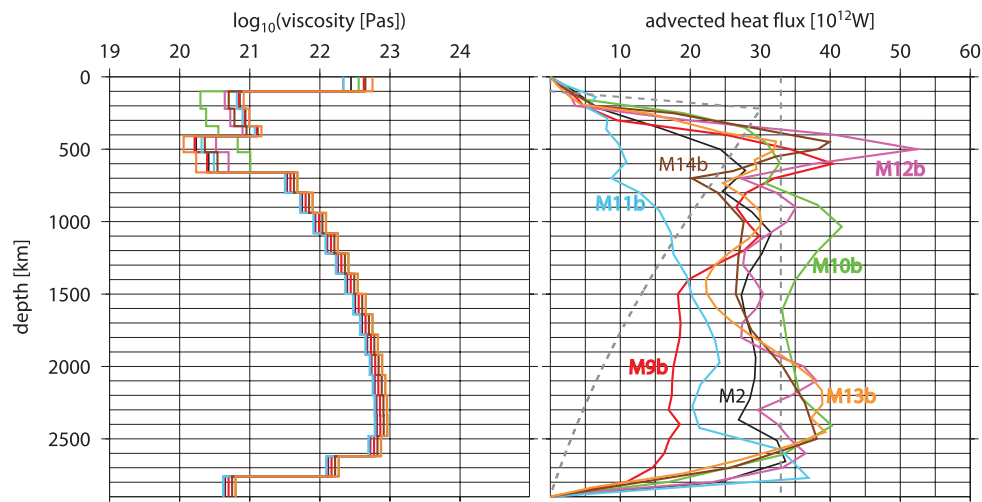
Figure 14. Optimized viscosity profiles (left) and heat flux profiles (right) for different tomography models. Other assumptions are as in model 2. Black: smean (Becker & Boschi 2002)—identical to the blue dotted line in Fig. 9; red: S20RTS (Ritsema & van Heijst 2000); green: SB4L18 (Masters *et al.* 2000); blue: model by Grand (2002); violet: SAW24B16 (Mégnin & Romanowicz 2000); orange: S12WM13 (Su *et al.* 1994); brown: S362D1 (Gu *et al.* 2001). Φ_{bh} and $\Phi_{ih}(r)$ are shown as grey dashed lines.
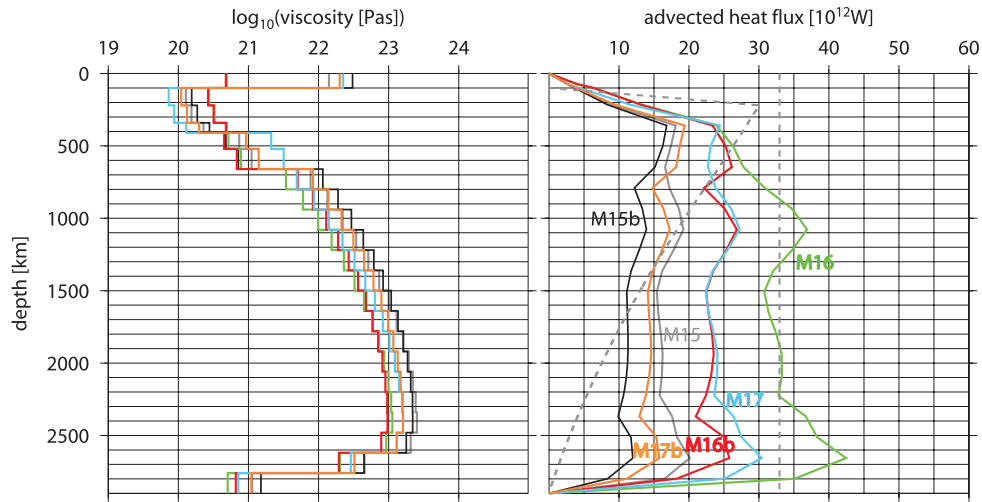
Figure 15. Optimized viscosity profiles (left) and heat flux profiles (right) for different surface boundary conditions. Fixed surface for reference case (grey) and model 2 (black); plates moving at half the speed of free plate motions, for tractions applied at the base of the lithosphere at 100 km depth for reference case (green) and model 2 (red); free plate motions for tractions applied at the surface, with additional penalty added to misfit function if computed rms surface plate motions differs from observed one for reference case (blue) and model 2 (orange). Φ_{bh} and $\Phi_{ih}(r)$ are shown as grey dashed lines.

14.8 per cent in cases M18 and M18b). This rather poor model performance arises, because plate-like surface motions do not naturally arise with a viscous rheology, and if they are artificially imposed, artefacts occur in the computed geoid, which degrade the fit. The optimized models in this case show rather low viscosities in the upper 100 km as in this way artefacts are kept small. Using stresses at depth 100 km for computing plate motions, if the model does not contain a high-viscosity lithosphere above, also appears inappropriate. We, therefore, go on to a case where we apply stresses at the surface. For this case, optimized models have very high viscosity in the uppermost 100 km and very slow plate motion; resulting sublithospheric viscosity and heat flux profiles are very similar to the fixed surface case shown. In the last case we, therefore, add

$$P_4 = (1 - v_{\mathrm{rms},c}/v_{\mathrm{rms},o})^2, \tag{35}$$

to the misfit function Π_2 in eq. (34), that is, penalizing if calculated and observed rms plate motions differ. Then we obtain for reference case parameters (M17, blue lines) a geoid variance reduction of 24 per cent, $v_{\mathrm{rms},c}$ is 4.0 cm yr^{-1} and plate motion (i.e. surface velocity) variance reduction 56 per cent. For model 2 parameters (M17b, orange lines) corresponding numbers are 31 per cent, 3.8 cm yr^{-1} and 58 per cent. Viscosities in the upper 100 km are a few times 10^{22} Pa s—as with a free surface in the three cases discussed that give a high geoid variance reduction—the reference case M1, model 2 (M2) and the case M3 with profiles from Calderwood (1999). For these three cases, $v_{\mathrm{rms},c}$ is 3.3, 5.0 and 4.6 cm yr^{-1}, surface velocity variance reduction is 28, −5 and 4 per cent. Thus, these models with free surface give approximately correct rms surface velocities even though these are not used as constraints; lithospheric viscosities (to be interpreted as effective viscosity along plate boundaries) required to obtain a good fit to the geoid are in the same range as those required to obtain appropriate plate speeds. These results do not change substantially if we penalize a misfit of rms plate motions as described. The smaller surface velocity variance reduction in models M1, M2 and M3 can be attributed to the fact that here surface velocities are not plate-like.

5 DISCUSSION AND CONCLUSIONS

5.1 Resulting viscosity profiles

We have derived here mantle viscosity profiles with a combination of mineral physics and mantle dynamics. They feature a strong viscosity increase with depth in the lower mantle up to about 10^{23} Pa s or slightly less above the D″ layer, several hundred times more than the viscosity low in the upper mantle. This is a larger viscosity contrast than previously inferred from the geoid constraint in global geodynamics (e.g. Thoraval & Richards 1997). We obtain this larger contrast because our resulting viscosity models have a characteristic hump in the lower mantle; preferred models feature a viscosity increase of about a factor 30 from below the 660 km discontinuity to the viscosity high in the lower mantle, and a viscosity decrease of somewhat more than a factor 100 from the viscosity high to the CMB. Models with much larger viscosity increase through the lower mantle tend to give a much higher misfit and are, therefore, considered less likely. Models with much larger viscosity decrease in the lowermost mantle also tend to give much higher misfit, unless the thermal boundary layer at the base of the mantle is much thinner. Because the highest viscosities are restricted to the deep mantle, they are also compatible with results from post-glacial rebound, which is rather insensitive to viscosities at that depth.

The combination of mineral physics, geoid and heat flux constraints applied here was motivated by the fact that the geoid alone does not place strong constraints on mantle viscosity structure (Thoraval & Richards 1997). However, we found that our model still leaves considerable uncertainties; for example, we cannot reliably distinguish whether the lowest viscosities occur in the asthenosphere or in the transition zone; generally, a somewhat better model fit occurs with lowest viscosities in the transition zone. This was e.g. also found by Marquart (2006). A possible explanation could be the presence of water in the transition zone (Smyth *et al.* 2004; Kavner 2003). Such a viscosity low serves to somewhat decouple flow in the upper and lower mantle, which appears to improve the fit to the geoid. However, this can also be achieved by narrow layers of low viscosity (Panasyuk & Hager 2000; Mitrovica & Forte 2004).

If we require the lowest viscosities to occur in the asthenosphere, then best-fit viscosity models look similar to the profile obtained by Mitrovica & Forte (2004) without mineral physics constraints. A difference is the narrow layer of low viscosity above depth 670 km which occurs in the model of Mitrovica & Forte (2004), and which is not possible with our parametrization.

With alternative surface boundary conditions (fixed or plate-like) the best-fit models have the lowest viscosity in the asthenosphere. Any indication of a viscosity low in the transition zone could, therefore, merely reflect the inappropriate surface boundary condition and neglect of lateral variations in rheology. However, this will need to be addressed by future studies.

5.2 Fit to the geoid

Our best-fit models with viscosity and scaling factor profiles based on mineral physics give a geoid variance reduction of about 80 per cent. This is similar to values achieved by previous authors, however, we were able to obtain this result in a parameter space that is rather small, as we use mineral physics to pre-constrain the viscosity structure and conversion factor from seismic velocities to densities. A variance reduction close to 80 per cent could be achieved for a range of modelling parameters, but not be substantially exceeded. With constant viscosities in upper mantle, transition zone and lower mantle, we obtain a slightly higher geoid variance reduction (81 per cent). However, we want to replace *ad hoc* assumptions (such as constant viscosities) by models based on mineral physics. We regard the outcome that this only leads to a slightly worse fit to the geoid, while at the same time a realistic heat flux profile (see discussion below) is maintained as quite satisfactory.

A geoid variance reduction of slightly more than 80 per cent appears to be the approximate limit that can be achieved with the interpretation of seismic wave speed anomalies purely in terms of thermal anomalies, and without consideration of lateral viscosity variations. Like Thoraval & Richards (1997), we obtained the best result with a free-slip surface boundary condition—probably, because this is the boundary condition that is consistent with the purely viscous rheology without lateral variations that we also use to model the lithosphere; plate-like surface velocities without lateral variations in rheology in the lithosphere lead to artefacts in the computed geoid.

The good fit to the geoid obtained is indicative that at depths where the geoid kernels (showing the sensitivity of the geoid to density variations) are comparatively large—away from the surface and CMB—seismic anomalies are primarily due to temperature anomalies. This leaves the regions close to the surface and close to the CMB as potential regions for large chemical variations: Our finding that the fit to the geoid is somewhat improved, if the conversion factor from seismic velocities to densities is reduced by about a factor 0.5 in the upper 220 km, may be additional evidence that part of the density anomalies in the uppermost mantle are due to compositional, rather than thermal anomalies. A more detailed treatment of the shallowest mantle would need to consider the non-linear dependence of seismic velocity on temperature anomalies; the same temperature variation causes larger *s* wave speed variation at lower temperature than at higher temperature (Cammarano *et al.* 2003).

On the other hand, surface velocity variance reduction obtained is highest with plate-like surface motions. This points towards the need of combining mineral physics constraints with geodynamic models that include lateral variations in rheology—particularly in the uppermost mantle (Čadek & Fleitout 2003).

5.3 Heat flux

In addition to a high geoid variance reduction, our best-fit models also give heat flux profiles that are compatible with the observation-based mantle heat flux. Heat flux profiles are quite variable for different density models—based on different mantle tomography models—used, but our best-fit models have a roughly constant heat flux through much of the mantle, corresponding to a mantle largely heated from below. The rather small fraction of plume heat flux compared to total surface heat flux has frequently been taken as evidence for a largely internally heated mantle. However, much higher values of plume flux have recently been inferred with the help of seismic tomography (Nolet *et al.* 2005). Experimental results (Jellinek *et al.* 2003) have shown that a significant fraction of core heat flux can be drawn into large-scale upwellings and is thus not observed at hotspots. A large part of core heat flux may be due to warming of slabs settling on the CMB (Yoshida & Ogawa 2005; Mittelstaedt & Tackley 2006). If seismic velocity anomalies are due to temperature anomalies, the skewness of *s*-wave tomography models suggests significant basal heating (Yanagisawa & Hamano 1999).

Predicted heat flux is generally too low in the uppermost few hundred km. This may be due to a number of reasons:

(i) The scaling factor in the uppermost 220 km has been arbitrarily reduced by a factor $F_l = 0.5$; the misfit becomes smaller for larger F_l (Fig. 12).

(ii) Heat flow in the lithosphere is dominated by diffusion, which is not included in our computation, and in many places the lithosphere is probably considerably thicker than the 100 km assumed here.

(iii) Probably a substantial fraction of heat flux occurs through subduction of lithospheric slabs, and those are not fully resolved in our model (expansion up to degree 31), especially in the upper mantle. Heat flow misfit P_2 for expansion up to degree $l_{max} = 31$ is less than for $l_{max} = 15$. The largest differences occur in the upper part of the mantle. Most density models used here to drive mantle flow are expanded to degree 31 or less, and we expect that P_2 would be further reduced if density and flow models were expanded to larger l_{max}.

(iv) Further heat flux at shorter wavelength may occur through small-scale convection, primarily in the regions with lowest viscosity. Since the remaining heat flux misfit is primarily in the depth region 100–400 km, small-scale convection could explain part of the misfit, especially if the lowest viscosities also occur in that depth range.

In our reference model, heat flux in the lower mantle tends to be somewhat too high. Better results are obtained in model 2, where temperature anomalies are less. While the amplitude of tomography models is currently not well constrained and the somewhat lower amplitudes required to obtain a better heat flux profile are probably within the range of uncertainties, this might also be an additional indication that some of the anomalies observed by seismic tomography are due to compositional, rather than temperature variations (Trampert *et al.* 2004).

5.4 Lowermost mantle

Lower boundary condition for the flow computations is a free surface at the CMB. For the optimized models we compute CMB topography and in particular excess ellipticity, which is constrained

by observations (Mathews *et al.* 2002). In the reference case, computed CMB excess ellipticity is eight times as large as observed, for both model 2 and the case with profiles from Calderwood (1999) it is seven times. We find generally that models that match heat flux profile and geoid well tend to imply CMB excess ellipticity several times larger than observed. We can reduce it to values compatible with observations if we choose sufficiently low viscosities of the lowermost mantle. However, in this case both the heat flux profile and geoid fit deteriorate to an unacceptable level. Within the model space considered, we were not able to obtain an acceptable fit to the geoid, heat flux profile and CMB excess ellipticity at the same time; for example, in the centre right panels of Figs 11 and 12 acceptable CMB excess ellipticity is only found in the top right corner, where both geoid and heat flux do not fit well. Results do not significantly change even if the excess ellipticity misfit is penalized in the optimization. Among the models considered we found the largest variation in predicted CMB excess ellipticity to be due to choosing different density models; among the tomography models included if Fig. 14, with other assumptions as in the reference case and model 2, predicted CMB topography varies between three and eight times the observed value. Forte *et al.* (1995) showed, using an older tomography model, that it is possible to modify the tomography model to fit excess ellipticity without significantly degrading the fit to the seismological data, and it remains to be tested whether this is still possible for the more recent tomography models considered here. The discrepancy may, however, also be due to chemical variations at the base of the mantle; if they occur close to the CMB they would be largely isostatically compensated and thus not strongly contribute to the geoid. On the other hand, stresses from overlying mantle flow could be largely compensated due to these chemical variations, and the topography at the CMB could be reduced to values compatible with the observed excess ellipticity (Steinberger & Holme 2006). Our preferred models have a temperature at the lower boundary of 3500 K, and a TBL thickness of 200 km. 3500 K is within the uncertainties of CMB temperatures inferred from experiments (Boehler 1996), but at the lower end. A possible explanation for this rather low temperature is again that there is chemically distinct material at the base of the mantle which is not, or only partly, entrained in flow in the overlying mantle, and the preferred temperature of about 3500 K does not actually correspond to CMB temperature, but temperature around the top of the chemically distinct material. The inferred high proportion of basal heating would not only include heat from the core but also from the chemically distinct layer. However, if dislocation creep is the dominant mechanism in the D″ layer, the same viscosity drop could result from a larger temperature increase in the D″ layer. Steinberger & Holme (2006) extend this geodynamic model to consider chemical variations within the lowermost ≈ 300 km of the mantle. In this case, the optimal TBL thickness shifts towards somewhat higher values around 300 km. Implications of the model presented here for the lowermost mantle are further complicated by the occurrence of a phase boundary recently found (Murakami *et al.* 2004). As its Clapeyron slope is currently not well known, it is, at present, difficult to implement into geodynamic models.

REFERENCES

Akaogi, M. & Ito, E., 1999. Calorimetric study on majorite-perovskite transition in the system $Mg_4Si_4O_{12}–Mg_3Al_2Si_3O_{12}$: transition boundaries with positive pressure-temperature slopes, *Phys. Earth planet. Inter.,* **114,** 129–140.

Akaogi, M., Ito, E. & Navrotsky, A., 1989. Olivine—modified spinel—spinel transitions in the system $Mg_2SiO_4 – Fe_2SiO_4$: calorimetric measurements, thermochemical calculations, and geophysical application, *J. geophys. Res.,* **94,** 15 671–15 685.

Albers, M. & Christensen, U.R., 2001. Channelling of plume flow beneath mid-ocean ridges, *Earth planet. Sci. Lett.,* **187,** 207–220.

Anderson, D.L. & Hart, R.S., 1978. Q of the Earth, *J. geophys. Res.,* **83,** 5869–5882.

Anderson, O.L., Oda, H. & Isaak, D., 1992. A model for the computation of thermal expansivity at high T and high compression: MgO as an example, *Geophys. Res. Lett.,* **19,** 1987–1990.

Bai, W., Vigny, C., Ricard, Y. & Froidevaux, C., 1992. On the origin of deviatoric stresses in the lithosphere, *J. geophys. Res.,* **97,** 11 729–11 737.

Becker, T.W. & Boschi, L., 2002. A comparison of tomographic and geodynamic mantle models, *Geochem. Geophys. Geosyst.,* **3,** 2001GC000168.

Becker, T.W. & O'Connell, R.J., 2001. Predicting plate velocities with mantle circulation models, *Geochem. Geophys. Geosyst.,* **2,** 2001GC000171.

Becker, T.W., Kellogg, J.B., Ekström, G. & O'Connell, R.J., 2003. Comparison of azimuthal seismic anisotropy from surface waves and finite-strain from global mantle-circulation models, *Geophys. J. Int.,* **155,** 696–714.

Behn, M., Conrad, C. & Silver, P.G., 2004. Detection of upper mantle flow associated with the African superplume, *Earth planet. Sci. Lett.,* **224,** 259–274.

Boehler, R., 1996. Melting temperature of the Earth's mantle and core: Earth's thermal structure, *Ann. Rev. Earth Planet. Sci.,* **24,** 15–40.

Čadek, O. & Fleitout, L., 2003. Effects of lateral viscosity variations in the top 300 km on geoid, dynamic topography and lithospheric stresses, *Geophys. J. Int.,* **152,** 566–580.

Čadek, O. & Fleitout, L., 2006. Effect of lateral viscosity variations in the core-mantle boundary region on predictions of the long-wavelength geoid, *Stud. Geophys. Geod.,* **50,** 217–232.

Calderwood, A.R., 1999. Mineral physics constraints on the temperature and composition of the Earth's mantle, *PhD thesis,* University of British Columbia, Dept. of Earth and Ocean Sciences, Canada.

Cammarano, F., Goes, S., Vacher, P. & Giardini, D., 2003. Inferring upper mantle temperatures from seismic velocities, *Phys. Earth planet. Inter.,* **138,** 197–222.

Christensen, U.R., 1983. Convection in a variable-viscosity fluid: Newtonian versus power-law rheology, *Earth planet. Sci. Lett.,* **64,** 153–162.

Chopelas, A. & Boehler, R., 1989. Thermal expansion measurements at very high pressure, systematics, and a case for a chemically homogeneous mantle, *Geophys. Res. Lett.,* **16,** 1347–1350.

Conrad, C.P. & Lithgow-Bertelloni, C., 2002. How mantle slabs drive plate tectonics, *Science,* **298,** 207–209.

Conrad, C.P. & Lithgow-Bertelloni, C., 2004. The relative importance of 'slab pull' and 'suction' as forces that drive plate motions, *J. geophys. Res.,* **109,** B10407.

Conrad, C.P. & Lithgow-Bertelloni, C., 2006. Influence of continental roots and asthenosphere on plate-mantle coupling, *Geophys. Res. Lett.,* **33,** L05312.

DeMets, C., Gordon, R.G., Argus, D.F. & Stein, S., 1990. Current plate motions, *Geophys. J. Int.,* **101,** 425–478.

Duffy, T.S. & Anderson, D.L., 1989. Seismic velocities in mantle minerals and the mineralogy of the upper mantle, *J. geophys. Res.,* **94,** 1895–1912.

Dziewonski, A.M. & Anderson, D.L., 1981. Preliminary Reference Earth Model, *Phys. Earth planet. Inter.,* **25,** 297–356.

Forte, A.M., Dziewonski, A.M. & Woodward, R.L., 1993. Aspherical structure of the mantle, tectonic plate motions, nonhydrostatic geoid, and topography of the core-mantle boundary, in *Dynamics of the Earth's Deep Interior and Earth Rotation,* Vol. 72, pp. 135–166, eds Le Mouël, J.-L., Smylie, D.E. & Herring, T., Geophys. Mon. Ser., AGU, Washington, DC.

Forte, A.M., Mitrovica, J.X. & Woodward, R.L., 1995. Seismic-geodynamic determination of the origin of excess ellipticity of the core-mantle boundary, *Geophys. Res. Lett.* **22,** 1013–1016.

Goes, S., Cammarano, F. & Hansen, U., 2004. Synthetic seismic signature of thermal mantle plumes, *Earth planet. Sci. Lett.,* **218,** 403–419.

Grand, S.P., 2002. Mantle shear-wave tomography and the fate of subducted slabs, *Philos. Trans. R. Soc. London, Ser. A,* **360,** 2475–2491.

Gu, Y.J., Dziewonski, A.M., Su, W. & Ekström, G., 2001. Models of the mantle shear velocity and discontinuities in the pattern of lateral heterogeneities, *J. geophys. Res.,* **106,** 11 169–11 199.

Gung, Y. & Romanowicz, B., 2004. Q tomography of the upper mantle using three-component long-period waveforms. *Geophys. J. Int.,* **157,** 813–830.

Hager, B.H. & O'Connell, R.J., 1979. Kinematic models of large-scale mantle flow, *J. geophys. Res.,* **84,** 1031–1048.

Hager, B.H. & O'Connell, R.J., 1981. A simple global model of plate dynamics and mantle convection, *J. geophys. Res.,* **86,** 4843–4867.

Haskell, N.A., 1935. The motion of a fluid under a surface load, 1, *Physics,* **6,** 265–269.

Hofmeister, A.M., 2005. Earth's heat flux revised and linked to chemistry, *Tectonophysics,* **395,** 159–177.

Ishii, M. & Tromp, J., 2004. Constraining large-scale mantle heterogeneity using mantle and inner-core sensitive normal modes, *Phys. Earth planet. Int.,* **146,** 113–124.

Ita, J.J. & Stixrude, L., 1992. Petrology, elasticity, and composition of the mantle transition zone, *J. geophys. Res.,* **97,** 6849–6866.

Iwamori, H., McKenzie, D. & Takahashi, E., 1995. Melt generation by isentropic mantle upwelling, *Earth planet. Sci. Lett.,* **134,** 253–266.

Jellinek, A.M., Gonnermann, H.M. & Richards, M.A., 2003. Plume capture by divergent plate motions: implications for the distribution of hotspots, geochemistry of mid-ocean ridge basalts, and estimates of the heat flux at the core-mantle boundary, *Earth planet. Sci. Lett.,* **205,** 361–378.

Kaban, M.K., Schwintzer, P. & Tikhotsky, S.A., 1999. A global isostatic gravity model of the Earth. *Geophys. J. Int.,* **136,** 519–536.

Karato, S., 1993. Importance of anelasticity in the interpretation of seismic tomography, *Geophys. Res. Lett.,* **20,** 1623–1626.

Karato, S., Zhang, S. & Wenk, H.R., 1995. Superplasticity in Earth's lower mantle: evidence from seismic anisotropy and rock physics, *Science,* **270,** 458–461.

Kavner, A., 2003. Elasticity and strength of hydrous ringwoodite at high pressure, *Earth planet. Sci. Lett.,* **214,** 645–654.

Kohlstedt, D.L. & Götze, C., 1974. Low-stress high-temperature creep in olivine single crystals, *J. geophys. Res.,* **79,** 2045–2051.

Lambeck, K. & Johnston, P., 1998. The viscosity of the mantle: evidence from analyses of glacial-rebound phenomena, in *The Earth's Mantle,* pp. 461–502, ed. Jackson, I., Cambridge University Press, Cambridge.

Lithgow-Bertelloni, C. & Richards, M.A., 1998. The dynamics of Cenozoic and Mesozoic plate motions, *Rev. Geophys.,* **36,** 27–78.

Lithgow-Bertelloni, C. & Silver, P.G., 1998. Dynamic topography, plate driving forces and the African superswell, *Nature,* **395,** 269–272.

Lithgow-Bertelloni, C. & Guynn, J.H., 2004. Origin of lithospheric stress field, *J. geophys. Res.,* **109,** B01408.

Marquart, G., 2006. Inferring mantle viscosity and *s*-wave-density conversion factor from new seismic tomography and geoid data, *Geophys. J. Int.,* submitted.

Masters, G., Laske, G., Bolton, H. & Dziewonski, A.M., 2000. The relative behavior of shear velocity, bulk sound speed, and compressional velocity in the mantle: implications for chemical and thermal structure, in *Earth's deep interior. Mineral physics and tomography from the atomic to the global scale,* Vol. 117, pp. 63–87, eds Karato, S., Forte, A.M., Liebermann, R.C., Masters, G. & Stixrude, L., Geophys. Mon. Ser., AGU, Washington, DC.

Mathews, P.M., Herring, T.A. & Buffett, B.A., 2002. Modeling of nutation and precession: new nutation series for nonrigid Earth and insights into the Earth's interior, *J. geophys. Res.,* **107,** doi:10.1029/2001JB000390.

Mégnin, C. & Romanowicz, B., 2000. The shear velocity structure of the mantle from the inversion of body, surface, and higher modes waveforms, *Geophys. J. Int.,* **143,** 709–728.

Mittelstaedt, E. & Tackley, P.J., 2006. Plume heat flow is much lower than CMB heat flow. *Earth planet. Sci. Lett.,* **241,** 202–210.

Mitrovica, J.X., 1996. Haskell [1935] revisited, *J. geophys. Res.,* **101,** 555–569.

Mitrovica, J.X. & Forte, A.M., 1997. Radial profile of mantle viscosity: results from the joint inversion of convection and postglacial rebound observables, *J. geophys. Res.,* **102,** 2751–2769.

Mitrovica, J.X. & Forte, A.M., 2004. A new inference of mantle viscosity based upon joint inversion of convection and glacial isostatic adjustment data, *Earth planet. Sci. Lett.,* **225,** 177–189.

Murakami, M., Hirose, K., Kawamura, K., Sata, N. & Ohishi, Y., 2004. Post-perovskite phase transition in $MgSiO_3$, *Science,* **304,** 855–858.

Nolet, G., Karato, S.-i. & Montelli, R., 2005. Plume fluxes from seismic tomography, *Geophys. Res. Abs.,* **7,** 04221.

Oganov, A.R., Brodholt, J.P. & Price, G.D., 2001. Ab initio elasticity and thermal equation of state of $MgSiO_3$ perovskite, *Earth planet. Sci. Lett.,* **184,** 555–560.

Panasyuk, S.V. & Hager, B.H., 2000. Inversion for mantle viscosity profiles constrained by dynamic topography and the geoid, and their estimated errors, *Geophys. J. Int.,* **143,** 821–836.

Panasyuk, S.V., Hager, B.H. & Forte, A.M., 1996. Understanding the effect of compressibility on geoid kernels, *Geophys. J. Int.,* **124,** 121–133.

Pari, G. & Peltier, W.R., 2000. Subcontinental mantle dynamics: a further analysis based on the joint constraints of dynamic surface topography and free-air gravity. *J. geophys. Res.,* **105,** 5635–5662.

Pari, G. & Peltier, W.R., 1995. Heat flow constraint on mantle convection, *J. geophys. Res.,* **100,** 12 731–12 751.

Pollack, H.N., Hurter, S.J. & Johnson, J.R., 1993. Heat loss from the Earth's interior: analysis of the global data set, *Rev. Geophys.,* **31,** 267–280.

Press, W.H., Flannery, B.P., Teukolski, S.A. & Vetterling, W.T., 1986. *Numerical Recipes—The Art of Scientific Computing (FORTRAN version),* Cambridge University Press, Cambridge.

Ranalli, G., 1995. *Rheology of the Earth,* 2nd edn, Chapman & Hall, London.

Ricard, Y. & Vigny, C., 1989. Mantle dynamics with induced plate tectonics, *J. geophys. Res.,* **94** 17 543–17 559.

Ricard, Y., Fleitout, L. & Froidevaux, C., 1984. Geoid heights and lithospheric stresses for a dynamic Earth, *Ann. Geophys.,* **2,** 267–286.

Richards, M.A. & Hager, B.H., 1984. Geoid anomalies in a dynamic Earth, *J. geophys. Res.,* **89,** 5987–6002.

Ritsema, J. & van Heijst, H.J., 2000. Seismic imaging of structural heterogeneity in Earth's mantle: evidence for large-scale mantle flow, *Sci. Progr.,* **83,** 243–259.

Schmeling, H., Marquart, G. & Ruedas, T., 2003. Pressure- and temperature-dependent thermal expansivity and the effect on mantle convection and surface observables, *Geophys. J. Int.,* **154,** 224–229.

Schubert, G., Turcotte, D.L. & Olson, P., 2001. *Mantle Convection in the Earth and Planets,* Cambridge University Press, Cambridge.

Smyth, J.R., Holl, C.M., Frost, D.J. & Jacobsen, S.D., 2004. High pressure crystal chemistry of hydrous ringwoodite and water in the Earth's interior, *Phys. Earth planet. Inter.,* **143–144,** 271–278.

Stacey, F.D., 1992. *Physics of the Earth,* 3rd edn, John Wiley & Sons, New York, NY.

Steinberger, B., 2000. Plumes in a convecting mantle: models and observations for individual hot-spots, *J. geophys. Res.,* **105,** 11 127–11 152.

Steinberger, B. & Holme, R., 2006. Mantle flow models with core-mantle boundary constraints: evidence for chemical heterogeneities in the lowermost mantle, *J. geophys. Res.,* submitted (available online at www.geodynamics.no/steinberger/steinberger_and_holme.pdf).

Steinberger, B., Schmeling, H. & Marquart, G., 2001. Large-scale lithospheric stress field induced by global mantle circulation, *Earth planet. Sci. Lett.,* **186,** 75–91.

Su, W., Woodward, R.L. & Dziewonski, A.M., 1994. Degree 12 model of shear velocity heterogeneity in the mantle, *J. geophys. Res.,* **99,** 6945–6980.

Thoraval, C. & Richards, M.A., 1997. The geoid constraint in global geodynamics: viscosity structure, mantle heterogeneity models and boundary conditions, *Geophys. J. Int.,* **131,** 1–8.

Trampert, J., Deschamps, F., Resovsky, J. & Yuen, D., 2004. Probabilistic tomography maps chemical heterogeneities throughout the lower mantle, *Science,* **306,** 853–856.

van Hunen, J., Zhong, S., Shapiro, N.M. & Ritzwoller, M.H., 2005. New evidence for dislocation creep from 3-D geodynamic modeling of the Pacific upper mantle structure, *Earth planet. Sci. Lett.,* **238,** 1–270.

White, R.S. & D. McKenzie, 1995. Mantle plumes and flood basalts, *J. geophys. Res.,* **100,** 17 543–17 585.

Wang, Z.W., 1999. The melting of Al-bearing perovskite at the core-mantle boundary. *Phys. Earth planet. Inter.,* **115,** 219–228.

Weertman, J. & Weertman, J.R., 1975. High temperature creep of rock and mantle viscosity. *Annu. Rev. Earth Planet. Sci.,* **3,** 293–315.

Wei, M. & Sandwell, D., 2006. Estimates of heat flow from Cenozoic seafloor using global depth and age data, *Tectonophysics,* **417,** 325–335.

Wessel, P. & Smith, W.H.F., 1998. New, improved version of the Generic Mapping Tools released, *EOS Trans. AGU,* **79,** 579.

Yamazaki, D. & Karato, S.-I., 2001. Some mineral physics constraints on the rheology and geothermal structure of Earth's lower mantle, *Am. Mineral.,* **86,** 385–391.

Yanagisawa, T. & Hamano, Y., 1999. 'Skewness' of S wave velocity in the mantle, *Geophys. Res. Lett.* **26,** 791–794.

Yoshida, M. & Ogawa, M., 2005. Plume heat flow in a numerical model of mantle convection with moving plates, *Earth planet. Sci. Lett.* **239,** 276–285.

Zerr, A. & Boehler, R., 1994. Constraints on the melting temperature of the lower mantle from high-pressure experiments on MgO and magnesiowüstite, *Nature,* **371,** 506–508.

Zhang, S. & Christensen, U., 1993. Some effects of lateral viscosity variations on geoid and surface velocities induced by density anomalies in the mantle, *Geophys. J. Int.,* **114,** 531–547.